

# Annealing Flow Generative Models Towards Sampling High-Dimensional and Multi-Modal Distributions

Dongze Wu, Yao Xie\*

## Abstract

Sampling from high-dimensional, multi-modal distributions remains a fundamental challenge across domains such as statistical Bayesian inference and physics-based machine learning. In this paper, we propose *Annealing Flow* (AF), a continuous normalizing flow-based approach designed to sample from high-dimensional and multi-modal distributions. The key idea is to learn a continuous normalizing flow-based transport map, guided by annealing, to transition samples from an easy-to-sample distribution to the target distribution, facilitating effective exploration of modes in high-dimensional spaces. Unlike many existing methods, AF training does not rely on samples from the target distribution. AF ensures effective and balanced mode exploration, achieves linear complexity in sample size and dimensions, and circumvents inefficient mixing times. We demonstrate the superior performance of AF compared to state-of-the-art methods through extensive experiments on various challenging distributions and real-world datasets, particularly in high-dimensional and multi-modal settings. We also highlight AF’s potential for sampling the least favorable distributions.

## 1 Introduction

Sampling from high-dimensional and multi-modal distributions is crucial for various fields, including physics-based machine learning like molecular dynamics (Miao et al., 2015; Salo-Ahen et al., 2020), quantum physics (Carlson et al., 2015; Lynn et al., 2019), and lattice field theory (Jay & Neil, 2021; Lozanovski et al., 2020). With modern datasets, it also plays a key role in Bayesian areas, including Bayesian modeling (Balandat et al., 2020; Kandasamy et al., 2018; Stephan et al., 2017) with applications in areas like computational biology (Overstall et al., 2020; Stanton et al., 2022), and Bayesian Neural Network sampling (Cobb & Jalaian, 2021; Izmailov et al., 2021).

*MCMC and Neural Network Variants:* Numerous MCMC methods have been developed over the past 50 years, including Metropolis-Hastings (MH) and its variants (Choi, 2020; Cornish et al., 2019; Griffin & Walker, 2013; Haario et al., 2001), Hamiltonian Monte Carlo (HMC) schemes (Bou-Rabee & Sanz-Serna, 2017; Girolami & Calderhead, 2011; Hoffman et al., 2021; Li et al., 2015; Shahbaba et al., 2014). HMC variants are still considered state-of-the-art methods. However, they require exponentially many steps in the dimension for mixing, even with just two modes (Hackett et al., 2021). More recently, Neural network (NN)-based sampling algorithms (Bonati et al., 2019; Egorov et al., 2024; Gu & Sun, 2020; Hackett et al., 2021; Li et al., 2021; Wolniewicz et al., 2024) have been developed to leverage NN expressiveness for improving MCMC, but they still inherit some limitations like slow mixing and imbalanced mode exploration, particularly in high-dimensional spaces.

*Annealing Variants:* Annealing methods (Gelfand et al., 1990; Neal, 2001; Sorkin, 1991; Van Groenigen & Stein, 1998) are widely used to develop MCMC techniques like Parallel Tempering (PT) and its variants (Chandra et al., 2019; Earl & Deem, 2005; Syed et al., 2022). In annealing, sampling gradually shifts from an easy distribution to the target by lowering temperature. Annealed Importance Sampling (Neal, 2001) and its variants (Chehab et al., 2024; Karagiannis & Andrieu, 2013; Zhang et al., 2021) are developed for estimating normalizing constants with low variance using MCMC samples from intermediate distributions. Recent Normalizing Flow and score-based annealing methods (Arbel et al., 2021; Doucet et al., 2022)

---

\*H. Milton Stewart School of Industrial and Systems Engineering (ISyE), Georgia Institute of Technology, Atlanta, GA 30332, USA. Email: dwu381@gatech.edu, yao.xie@isye.gatech.edu.

optimize intermediate densities for lower-variance estimates, but still rely on MCMC for sampling. However, MCMC struggles with slow mixing, local mode trapping, mode imbalance, and correlated samples issues. These limitations are particularly pronounced in high-dimensional, multi-modal settings (Hackett et al., 2021; Van Ravenzwaaij et al., 2018).

*Particle Optimization Methods:* Recently, particle-based optimization methods have emerged for sampling, including Stein Variational Gradient Descent (SVGD) (Liu & Wang, 2016), and stochastic approaches such as (Dai et al., 2016; Detommaso et al., 2018; Li et al., 2023; Liu, 2017; Maddison et al., 2018; Nitanda & Suzuki, 2017; Pulido & van Leeuwen, 2019). However, many of these methods rely on kernel computations, which scale polynomially with sample size, and are sensitive to hyperparameters.

*Normalizing Flows:* Recently, discrete Normalizing Flows (NFs) (Rezende & Mohamed, 2015) and Stochastic NFs (Hagemann et al., 2022; Wu et al., 2020) have been actively explored for sampling tasks. Discrete NFs often suffer from mode collapse, and methods relying on them (Albergo & Vanden-Eijnden, 2023; Arbel et al., 2021; Brofos et al., 2022; Cabezas et al., 2024; Gabri e et al., 2021, 2022; Matthews et al., 2022) attempt to mitigate this issue using MCMC corrections. Most recently, Fan et al.; Tian et al. (2024) introduced path-guided NFs, which utilize training losses conceptually similar to score matching. However, these methods require a substantial number of discretized time steps, with score estimation at each step. Besides, the quality of these estimations significantly influences the overall training performance.

Challenges persist with multi-modal distributions in high-dimensional spaces. This paper introduces *Annealing Flow* (AF), a novel sampling scheme that learns a continuous normalizing flow map from an easy-to-sample distribution  $\pi_0(x)$  to the target  $q(x)$ , guided by annealing time steps. The training loss is formulated based on Dynamic Optimal Transport (OT). Our key contributions are as follows:

- The unique dynamic OT objective in AF enables training with significantly fewer intermediate time steps compared to the most recent annealing-like NF approaches (Fan et al.; Tian et al., 2024), which rely on score estimation for their training loss. Additionally, the incorporation of Wasserstein regularization into the dynamic OT loss greatly enhances stability, leading to more stable performance than other methods.
- The annealing procedure in our algorithm enables successful handling of high-dimensional distributions with widely separated modes. In challenging experimental settings, our method outperforms state-of-the-art approaches, including NF-based methods (Arbel et al., 2021; Fan et al.; Matthews et al., 2022; Tian et al., 2024), while requiring significantly fewer training time steps.
- From a theoretical perspective, we establish in Proposition 4 that the infinitesimal optimal velocity field corresponds to the score difference between consecutive annealing densities. This is a distinctive property of our dynamic OT-based objective, setting it apart from the most recent Annealing-like methods (Fan et al.; Tian et al., 2024). Furthermore, we demonstrate the equivalence of AF’s objective to the Wasserstein Gradient Flow, along with its associated convergence theorems, in Appendix B.

## 2 Preliminaries

*Neural ODE and Continuous Normalizing Flow:* A Neural ODE is a continuous model where the trajectory of data is modeled as the solution of an ordinary differential equation (ODE). Formally, in  $\mathbb{R}^d$ , given an input  $x(t_0) = x_0$  at time  $t_0$ , the transformation to the output  $x(T)$  is governed by:

$$\frac{dx(t)}{dt} = \mathbf{v}(x(t), t), \tag{1}$$

where  $\mathbf{v}(x(t), t)$  represents the velocity field, which is of the same dimension as  $x(t)$  and is parameterized by a neural network with input  $x(t)$  and  $t$ .

A Continuous Normalizing Flow (CNF) is a class of normalizing flows where the transformation of a probability density from a base distribution  $p(x)$  (at  $t = 0$ ) to a target distribution  $q(x)$  (at  $t = T$ ) is governed by a Neural ODE. The marginal density of  $x(t)$ , denoted as  $\rho(x, t)$ , evolves according to the continuity equation derived from the ODE in Eq. (1). This continuity equation is written as:

$$\partial_t \rho(x, t) + \nabla \cdot (\rho(x, t) \mathbf{v}(x, t)) = 0, \quad \rho(x, 0) = p(x), \tag{2}$$

where the divergence  $\nabla \cdot (\rho v)$  accounts for the change in density as the flow evolves over time.

*Dynamic Optimal Transport (OT)*: The Benamou-Brenier equation (Benamou & Brenier, 2000) below provides the dynamic formulation of Optimal Transport  $\mathcal{T}$ .

$$\begin{aligned} & \inf_{\rho, v} \int_0^1 \mathbb{E}_{x(t) \sim \rho(\cdot, t)} \|\mathbf{v}(x(t), t)\|^2 dt \\ & \text{s.t. } \partial_t \rho + \nabla \cdot (\rho v) = 0, \quad \rho(\cdot, 0) = p, \quad \rho(\cdot, 1) = q, \end{aligned} \quad (3)$$

The optimization problem seeks to find the optimal transport map that moves mass from the base density  $p$  to the target density  $q$ , subject to the continuity equation (2) to ensure that  $\rho(\cdot, t)$  evolves as a valid probability density over time. Additionally, the constraint  $\rho(\cdot, 1) = q$  ensures that the target density is reached by the end of the time horizon. The time horizon is scaled to  $[0, 1]$ .

### 3 Annealing Flow Model

The annealing philosophy (Gelfand et al., 1990; Neal, 2001; Sorkin, 1991; Van Groenigen & Stein, 1998) refers to gradually transitioning an initial flattened distribution to the target distribution as the temperature decreases. Building on this idea, we introduce Annealing Flow (AF), a sampling algorithm that learns a continuous normalizing flow to gradually map an initial easy-to-sample density  $\pi_0(x)$  to the target density  $q(x)$  through a set of intermediate distributions.

We define  $q(x) = Z\tilde{q}(x)$  where  $\tilde{q}(x)$  represents the unnormalized target distribution given in explicit form. Next, we define a sequence of intermediate distributions  $f_k(x)$  that interpolate between an easy-to-sample initial distribution  $\pi_0(x)$  (e.g., a Gaussian) and the target  $q(x)$ . These intermediate distributions are formulated as:

$$f_k(x) = \pi_0(x)^{1-\beta_k} q(x)^{\beta_k} = Z_k \tilde{f}_k(x), \quad (4)$$

Here  $\tilde{f}_k(x) = \pi_0(x)^{1-\beta_k} \tilde{q}(x)^{\beta_k}$ , and  $\beta_k$  is an increasing sequence with  $\beta_0 = 0$  and  $\beta_K = 1$ . This formulation ensures that  $\tilde{f}_0(x) = \pi_0(x)$  and  $\tilde{f}_K(x) = \tilde{q}(x)$ . The sequence  $0 = \beta_0 < \beta_1 < \dots < \beta_K = 1$  controls the gradual transition between the two distributions.

The above construction aligns with the annealing philosophy. As  $\beta_k$  increases,  $\tilde{f}_k(x)$  gradually sharpens toward the target  $\tilde{q}(x)$ , starting from the initially flattened distribution around  $\pi_0(x)$ . These annealed densities serve as a bridge, providing a gradual flow path from the easy-to-sample distribution  $\pi_0(x)$  to the target density  $q(x)$ . Figure 1 provides an intuitive illustration of this process, where  $\pi_0(x)$  is a standard Gaussian, and  $q(x)$  is a Gaussian mixture model with six modes.

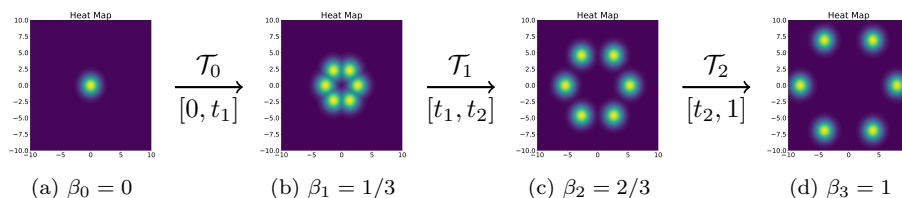


Figure 1: Illustration of the Annealing Flow Map, with a set of intermediate distributions from  $\pi_0(x) = N(0, I_2)$  to  $q(x)$ , a GMM with 6 modes.

#### 3.1 Optimal transport map

We aim to learn a continuous optimal transport map between an easy-to-sample distribution  $\pi_0(x)$  and the target distribution  $q(x)$ . Once trained, users simply sample  $\{x^{(i)}(0)\}_{i=1}^n \sim \pi_0(x)$ , and the transport map pushes them to  $\{x^{(i)}(1)\}_{i=1}^n \sim q(x)$ . The transport map  $\mathcal{T}$  evolves the density according to (2), which in turn drives the evolution of the sample  $x(t)$  following the ODE in (1):

$$\mathcal{T}(x(t)) = x(0) + \int_0^t \mathbf{v}(x(s), s) ds, \quad t \in [0, 1]. \quad (5)$$

We divide the time horizon  $[0, 1]$  of  $\mathcal{T}$  into  $K$  intervals  $[t_{k-1}, t_k]$  for  $k = 1, 2, \dots, K$ , where  $t_0 = 0$  and  $t_K = 1$ . Guided by the annealing flow path defined in (4), the continuous flow map  $\mathcal{T}$  gradually transforms the density from  $f_0(x)$  to  $f_1(x)$  over  $[0, t_1]$ , and continues this process until  $f_{K-1}(x)$  is transformed into  $f_K(x) = q(x)$  over  $[t_{K-1}, t_K]$ . Figure 1 shows this progression with two intermediate distributions. For clarity, we denote  $\mathcal{T}_k(x)$  as the segment of the continuous normalizing flow during  $[t_{k-1}, t_k]$ , which pushes the density from  $f_{k-1}(x)$  to  $f_k(x)$ .

### 3.2 Objective of annealing flow net

Annealing Flow aims to learn each transport map  $\mathcal{T}_k$  based on dynamic OT objective (3) over the time horizon  $[t_{k-1}, t_k]$ , where the velocity field  $\mathbf{v}_k(x(t), t)$  is learned using a neural network. The terminal condition  $\rho(\cdot, 1) = q$  in (3) can be relaxed by introducing a Kullback–Leibler (KL) divergence term (see, for instance, Ruthotto et al. (2020)). Consequently, minimizing the objective (3) for dynamic optimal transport  $\mathcal{T}_k : f_{k-1}(x) \rightarrow f_k(x)$  can be reduced to solving the following problem:

$$\mathcal{T}_k = \arg \min_{\mathcal{T}} \left\{ \text{KL}(\mathcal{T}_{\#} f_{k-1} \| f_k) + \gamma \int_{t_{k-1}}^{t_k} \mathbb{E}_{x(t) \sim \rho_k(\cdot, t)} \|\mathbf{v}_k(x(t), t)\|^2 dt \right\}, \quad (6)$$

subject to  $\rho_k(x(t), t)$  and  $\mathbf{v}_k(x(t), t)$  evolving according to (2). Here,  $\gamma > 0$  is a regularization parameter,  $\mathbf{v}_k(x(t), t)$  denotes the velocity field during the  $k$ -th time interval  $[t_{k-1}, t_k]$ , and  $\text{KL}(\mathcal{T}_{\#} f_{k-1} \| f_k)$  represents the KL divergence between the push-forward density  $\mathcal{T}_{\#} f_{k-1}$  and the target density  $f_k$ . Additionally, the constraint (2) ensures that  $x(t)$  follows the ODE trajectory defined by (1) during  $t \in [t_{k-1}, t_k]$ , which is given by:

$$x(t) = x(t_{k-1}) + \int_{t_{k-1}}^t \mathbf{v}_k(x(s), s) ds, \quad t \in [t_{k-1}, t_k]. \quad (7)$$

We can rewrite  $\tilde{f}_k(x) = Z e^{E_k(x)}$ , where  $E_k(x)$  is the energy function, with the associated unnormalized energy given by  $\tilde{E}_k(x) = -\log \tilde{f}_k$ . The following proposition shows that once we have obtained samples from  $f_{k-1}(x)$ , the KL divergence in (6) can be computed exactly based on  $\mathbf{v}_k(x(t), t)$  and  $\tilde{E}_k(x)$ . Therefore, learning an optimal transport map  $\mathcal{T}_k$  reduces to learning the optimal  $\mathbf{v}_k(x(t), t)$ . The proof is provided in Appendix A.1.

**Proposition 1** (KL-Divergence Decomposition) *Given the unnormalized density  $f_{k-1}$ , the KL-Divergence between  $\mathcal{T}_{\#} f_{k-1}$  and  $f_k$  is equivalent to:*

$$\text{KL}(\mathcal{T}_{\#} f_{k-1} \| f_k) = c + \mathbb{E}_{x(t_{k-1}) \sim f_{k-1}} \left[ \tilde{E}_k(x(t_k)) - \int_{t_{k-1}}^{t_k} \nabla \cdot \mathbf{v}_k(x(s), s) ds \right], \quad (8)$$

up to a constant  $c$  that is independent of  $\mathbf{v}_k(x(s), s)$ .

Given  $x(t_{k-1})$  from  $f_{k-1}(x)$ , the value of  $x(t_k)$  inside the energy function  $\tilde{E}_k$  can be calculated as shown in equation (7). Additionally, according to the proposition below, the second term in the objective (6) can be relaxed as a discretized sum. The proof is provided in Appendix A.1.

**Proposition 2** (Wasserstein Distance Discretization) *Let  $x(t)$  be particle trajectories driven by a smooth velocity field  $\mathbf{v}_k(x(t), t)$  over the time interval  $[t_{k-1}, t_k]$ , where  $h_k = t_k - t_{k-1}$ . Assume that  $\mathbf{v}_k(x, t)$  is Lipschitz continuous in both  $x$  and  $t$ . By dividing  $[t_{k-1}, t_k]$  into  $S$  equal mini-intervals with grid points  $t_{k-1, s}$  (where  $s = 0, 1, \dots, S$  and  $t_{k-1, 0} = t_{k-1}$ ,  $t_{k-1, S} = t_k$ ), we have:*

$$\int_{t_{k-1}}^{t_k} \mathbb{E}_{x(t)} [\|\mathbf{v}_k(x(t), t)\|^2] dt = \frac{S}{h_k} \sum_{s=0}^{S-1} \mathbb{E} [\|x(t_{k-1, s+1}) - x(t_{k-1, s})\|^2] + O(h_k^2/S). \quad (9)$$

As  $h_k \rightarrow 0$  or  $S \rightarrow \infty$ , the error term  $O(h_k^2/S)$  becomes negligible.



One can observe that the RHS of (9) can be interpreted as the discretized sum of the squared Wasserstein-2 distance. The dynamic  $W_2$  regularization encourages smooth transitions from  $f_{k-1}$  to  $f_k$  with minimal transport cost, promoting efficient mode exploration.

Next, by incorporating Propositions 1 and 2 into objective (6), the *final objective* becomes:

$$\min_{\mathbf{v}_{\mathbf{k}}(\cdot, t)} \mathbb{E}_{x(t_{k-1}) \sim f_{k-1}} \left[ \tilde{E}_k(x(t_k)) - \int_{t_{k-1}}^{t_k} \nabla \cdot \mathbf{v}_{\mathbf{k}}(x(s), s) ds + \alpha \sum_{s=0}^{S-1} \|x(t_{k-1, s+1}) - x(t_{k-1, s})\|^2 \right]. \quad (10)$$

Here,  $\alpha = \gamma S/h_k$  and  $\mathbf{v}_{\mathbf{k}}(x(s), s)$  is learned by a neural network. We break the time interval  $[t_{k-1}, t_k]$  into  $S$  mini-intervals, and  $x(t_{k-1, s+1})$  is computed as in equation (7).

After learning, connecting the Annealing Flow nets together yields a smooth flow map  $\mathcal{T} : \mathcal{T}_1 \rightarrow \mathcal{T}_2 \rightarrow \dots \rightarrow \mathcal{T}_K$ , which transforms samples from  $\pi_0(x)$  to the target  $q(x)$ . Please see Section 4.2 for efficient sampling of Annealing Flow and its comparisons with other sampling methods.

### 3.3 Properties of learned velocity field

The objective in (10) can be reformulated as shown below when  $h_k = t_k - t_{k-1} \rightarrow 0$ . The proof is provided in Appendix A.2.

**Proposition 3** (Objective Reformulation) *Denote  $h_k = t_k - t_{k-1}$ , and let  $\mathbf{s}_{\mathbf{k}} = \nabla \log f_{\mathbf{k}}(x)$  denote the score function of  $f_{\mathbf{k}}$ . As  $h_k \rightarrow 0$ , the objective in (10) becomes equivalent to the following:*

$$\min_{\mathbf{v}_{\mathbf{k}} = \mathbf{v}_{\mathbf{k}}(\cdot, 0)} \mathbb{E}_{x \sim f_{k-1}} \left[ -T_{f_k} \mathbf{v}_{\mathbf{k}} + \frac{1}{2} \|\mathbf{v}_{\mathbf{k}}\|^2 \right], \quad T_{f_k} \mathbf{v}_{\mathbf{k}} := \mathbf{s}_{\mathbf{k}} \cdot \mathbf{v}_{\mathbf{k}} + \nabla \cdot \mathbf{v}_{\mathbf{k}}. \quad (11)$$

Define  $L^2(f_{k-1}) = \{v : \mathbb{R}^d \rightarrow \mathbb{R}^d \mid \int_{\mathbb{R}^d} \|\mathbf{v}(x)\|^2 f_{k-1}(x) dx < \infty\}$  as the  $L^2$  space over  $(\mathbb{R}^d, f_{k-1}(x)dx)$ . We can then establish the following property, with proofs provided in Appendix A.2:

**Proposition 4** (Optimal Velocity Field as Score Difference) *Suppose  $h_k \rightarrow 0$ . Let  $f_{k-1}$  and  $f_k$  be continuously differentiable on  $\mathbb{R}^d$ . Assume that  $\nabla \cdot \mathbf{v}_{\mathbf{k}}(x)$  exists for all  $x \in \mathbb{R}^d$ , and  $\nabla \cdot \mathbf{v}_{\mathbf{k}}(x)$ ,  $\mathbf{s}_{\mathbf{k}-1}$  and  $\mathbf{s}_{\mathbf{k}}$  belong to  $L^2(f_{k-1})$ . Assume that the components of  $\mathbf{v}_{\mathbf{k}}$  are independent and  $\lim_{\|x\| \rightarrow \infty} f_{k-1}(x) \|\mathbf{v}_{\mathbf{k}}(x)\|_2 = 0$ . Under these conditions, the minimizer of (10) is:*

$$\mathbf{v}_{\mathbf{k}}^* = \mathbf{s}_{\mathbf{k}} - \mathbf{s}_{\mathbf{k}-1}. \quad (12)$$

Therefore, the infinitesimal optimal  $\mathbf{v}_{\mathbf{k}}^*$  is equal to the difference between score function of the next density,  $f_k$ , and the current density,  $f_{k-1}$ . This suggests that when the two intermediate densities are sufficiently close, i.e., when the number of  $\beta_k$  is large enough, the optimal velocity field equals the difference between the score functions. By adding more intermediate densities, one can construct a sufficiently smooth transport map  $\mathcal{T}$  that exactly learns the mapping between each pair of densities.

Additionally, one can observe that when each  $f_k(x)$  is set to the target  $q(x)$ , i.e., when all  $\beta_k$  are set to 1, and the second term in the objective (6) is relaxed to static  $W_2$  regularization, the objective of Annealing Flow becomes equivalent to Wasserstein gradient flow. This is detailed in Appendix B.

## 4 Training and Sampling of Annealing Flow Net

### 4.1 Block-wise training

Training of the  $k$ -th flow map in Annealing Flow begins once the  $(k-1)$ -th block has completed training. Given the samples  $\{x^{(i)}(t_{k-1})\}_{i=1}^n \sim f_{k-1}(x)$  produced after the  $(k-1)$ -th block, we can replace  $\mathbb{E}_{x \sim f_{k-1}}$  with the empirical average. The divergence of the velocity field can be computed either by brute force or via the Hutchinson trace estimator (Hutchinson, 1989; Xu et al., 2024b):

$$\nabla \cdot \mathbf{v}_{\mathbf{k}}(x, t) \approx \mathbb{E}_{\epsilon \sim N(0, I_d)} \left[ \epsilon^T \frac{\mathbf{v}_{\mathbf{k}}(x + \sigma \epsilon, t) - \mathbf{v}_{\mathbf{k}}(x, t)}{\sigma} \right]. \quad (13)$$

This approximation becomes exact as  $\sigma \rightarrow 0$ . Further details are provided in C.2. Additionally, we apply the Runge-Kutta method for numerical integration, with details provided in C.3.

Our algorithm uses a block-wise training of the continuous normalizing flow map. Specifically, the training of Annealing Flow is summarized in Algorithm 1. The block-wise training approach of Annealing Flow significantly reduces memory and computational requirements, as only one neural network is trained at a time, independent of the other flow networks.

---

**Algorithm 1** Block-wise Training of Annealing Flow Net

---

**Require:** Unnormalized target density  $\tilde{q}(x)$ ; an easy-to-sample  $\pi_0(x)$ ;  $\{\beta_1, \beta_2, \dots, \beta_{K-1}\}$ ; Total number of blocks  $K$ .

- 1: Set  $\beta_0 = 0$  and  $\beta_K = 1$
- 2: For  $k = 1, 2, \dots, K$ :
- 3:   Set  $f_k(x) = \pi_0(x)^{1-\beta_k} \tilde{q}(x)^{\beta_k}$ ;
- 4:   Sample  $\{x^{(i)}(t_0)\}_{i=1}^n$  from  $\pi_0(x)$ ;
- 5:   Compute the pushed samples  $x^{(i)}(t_{k-1})$  from the trained  $(k-1)$  blocks via (14);
- 6:   Optimize  $\mathbf{v}_k(\cdot, t)$  upon minimizing the objective function.

(Optional Refinement Blocks)

- 7: For  $k = K + 1, K + 2, \dots, L$ :
  - 8:   Set  $\beta_k = 1$  and optimize  $\mathbf{v}_k(\cdot, t)$  following the procedures outlined above.
- 

## 4.2 Efficient sampling and comparisons with other methods

Once the continuous normalizing flow map  $\mathcal{T}$  is learned, the sampling process of the target  $q(x)$  can be very efficient. Users can simply sample  $\{x^{(i)}(t_0 = 0)\}_{i=1}^n$  from  $\pi_0(x)$ , and then directly calculate  $\{x^{(i)}(t_K = 1)\}_{i=1}^n \sim q(x)$  through Annealing Flow nets:

$$x^{(i)}(t_k) = \mathcal{T}_k(x^{(i)}(t_{k-1})) = x^{(i)}(t_{k-1}) + \int_{t_{k-1}}^{t_k} \mathbf{v}_k(x^{(i)}(s), s) ds, \quad k = 1, 2, \dots, K. \quad (14)$$

Figure 2 provides an illustrative example of Annealing Flow (AF), alongside other Normalizing Flows (NFs) methods — CRAFT (Matthews et al., 2022), LFIS (Tian et al., 2024), and PGPS (Fan et al.) as well as Hamiltonian Monte Carlo (HMC) and Parallel Tempering (PT). MCMC requires long mixing times when sampling from complex distributions. In contrast, NFs directly push samples from  $\pi_0(x)$  through the learned transport map, enabling faster sampling, especially for large sample sizes. MCMC also generates correlated samples, as each new sample depends on the previous one, reducing the effective sample size (ESS) and efficiency. AF avoids this by producing independent samples, improving overall sample quality.

Among the NF methods, we note that for more challenging distributions, CRAFT, as well as score-matching-based methods such as LFIS and PGPS, require significantly more intermediate time steps than AF to achieve comparable performance. This is thoroughly discussed in Section 6 and Appendix D.

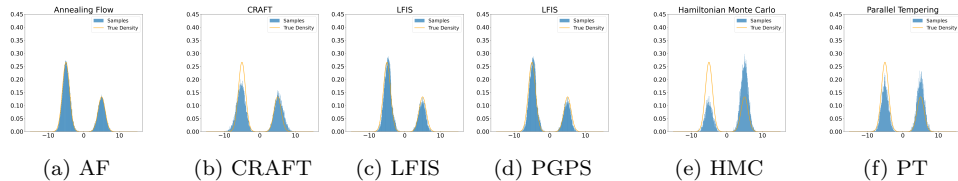


Figure 2: Illustrative Example: Comparison of different sampling methods for the density  $p(x) = \frac{2}{3}N(-5, 1) + \frac{1}{3}N(5, 1)$

Compared to MCMC, we comment that Annealing Flow indeed needs more expensive pre-training than MCMC, which, however, can be done offline and only needs to be done once and then deployed for sampling. Once trained, AF samplers are highly efficient, generating 10,000 samples in an average of 2.1 seconds in our challenging 50-dimensional experiment. The training efficiency is further discussed in Appendix D.2.

## 5 Importance Flow

Sampling from complex distributions is fundamental, which can benefit tasks like normalizing constant estimation, Bayesian analysis, and various machine learning problems. Here, we briefly discuss another aspect: using Annealing Flow to sample from the Least-Favorable-Distribution (LFD) and obtain a low-variance Importance Sampling (IS) estimator, referred to as Importance Flow.

### 5.1 Settings

Suppose we want to estimate  $\mathbb{E}_{X \sim \pi_0(x)} [h(X)]$ , which cannot be computed in closed form. A natural approach is to use Monte Carlo estimation by sampling  $\{x_i\}_{i=1}^n$  from  $\pi_0(x)$ . However, if  $x_i$  consistently falls in regions where  $h(x)$  has extreme values, the estimator may exhibit high variance. For example, with  $\pi_0(x) = N(0, I_d)$  and  $h(x) = 1_{\|x\| \geq 6}$ , almost no samples will satisfy  $\|x\| \geq 6$ , resulting in a zero estimate.

To address this situation, we can select an appropriate proposal distribution  $q(x)$  and rewrite the expectation and MC estimator as:

$$\mathbb{E}_{x \sim \pi_0(x)} [h(x)] = \mathbb{E}_{x \sim q(x)} \left[ \frac{\pi_0(x)}{q(x)} h(x) \right] \approx \frac{1}{n} \sum_{i=1}^n \frac{\pi_0(x_i)}{q(x_i)} h(x_i), \quad x_i \sim q(x). \quad (15)$$

It is well-known that the theoretically optimal proposal for the importance sampler is:  $q^*(x) \propto \pi_0(x)|h(x)| := \tilde{q}^*(x)$ . However, given the definition of  $\tilde{q}^*(x)$ , it is often difficult to sample from, especially when  $\pi_0(x)$  or  $h(x)$  is complex. Consequently, people typically choose a distribution that is similar in shape to the theoretically optimal proposal but easier to sample from.

Annealing Flow enables sampling from  $q^*(x)$ , allowing the construction of an Importance Sampling (IS) estimator. However,  $q^*(x)$  is only known up to the normalizing constant  $Z$ , where  $q^*(x) = \frac{1}{Z} \tilde{q}^*(x)$  and  $Z = \mathbb{E}_{x \sim \pi_0(x)} [h(x)]$  is our target. Therefore, assuming no knowledge on  $Z$ , a common choice can be the Normalized IS Estimator:  $\hat{I}_N = \sum_{i=1}^n \frac{\pi_0(x_i)}{\tilde{q}(x_i)} h(x_i) / \sum_{i=1}^n \frac{\pi_0(x_i)}{\tilde{q}(x_i)}$ . However, this estimator is often biased, as can be seen from Jensen’s Inequality.

### 5.2 Density ratio estimation

Using samples from  $q^*(x)$  and those along the trajectory obtained via Annealing Flow, we can train a neural network for Density Ratio Estimation (DRE) of  $\frac{\pi_0(x)}{q^*(x)}$ . Inspired by works Choi et al. (2022); Rhodes et al. (2020); Xu et al. (2023), we can train a continuous neural network  $r(x) = r_K(x; \theta_K) \circ r_{K-1}(x; \theta_{K-1}) \circ \dots \circ r_1(x; \theta_1)$ , where samples  $x_i \sim f_K = q^*(x)$  are inputs and the output is the density ratio  $\frac{\pi_0(x_i)}{q^*(x_i)}$ . Each  $r_k(x; \theta_k)$  is trained using the following loss:

$$\mathcal{L}_k(\theta_k) = \mathbb{E}_{x(t_{k-1}) \sim f_{k-1}} \left[ \log(1 + e^{-r_k(x_i(t_{k-1})))} \right] + \mathbb{E}_{x(t_k) \sim f_k} \left[ \log(1 + e^{r_k(x_i(t_k))}) \right].$$

After successful training,  $r_k^*(x) = \log \frac{f_{k-1}(x)}{f_k(x)}$ , and thus  $r^*(x) = \sum_{k=1}^K r_k^*(x) = \log \frac{\pi_0(x)}{q^*(x)}$ . Please refer to Appendix A.3 and C.5 for the proof and further details. To obtain the optimal importance sampling estimator, we can then directly use samples  $\{x_i\}_{i=1}^n \sim q^*(x)$  from Annealing Flow and apply (15) together with the DRE:  $\frac{1}{n} \sum_{i=1}^n \exp(r^*(x_i)) \cdot h(x_i)$ . The estimator is unbiased and can achieve zero variance theoretically.

## 6 Numerical Experiments

In this section, we present numerical experiments comparing Annealing Flow (AF) with the following methods: (1) Annealing-based MCMC: Parallel Tempering (PT); (2) Particle Optimization methods: Stein Variational Gradient Descent (SVGD) (Liu & Wang, 2016) and Mollified Interaction Energy Descent (MIED) (Li et al., 2023); (3) NN-assisted MCMC: AI-Sampler (AIS) (Egorov et al., 2024); and (4) Normalizing Flow approaches: Continual Repeated Annealed Flow Transport Monte Carlo (CRAFT) (Matthews et al., 2022), Liouville Flow Importance Sampler (LFIS) (Tian et al., 2024), and Path-Guided Particle-based Sampling

(PGPS) (Fan et al.). Experimental details are provided in Section C.3. Our code is publicly available on <https://github.com/StatFusion/Annealing-Flow-For-Sampling>.

For the Gaussian Mixture Models (GMMs) experiments, the number of time steps for our AF is set to 10, using 8 intermediate densities and 2 refinement blocks. For funnel distributions, 8 time steps are employed, with each intermediate density serving as the target. For Exp-Weighted Gaussian, 20 time steps are used, with 15 intermediate densities and 5 refinement blocks. Notably, methods like CRAFT, LFIS, and PGPS require up to 256 time steps to achieve satisfactory performance.

To ensure fair comparisons, the figures and tables (except Table 4) in the main manuscript use the same number of training steps and intermediate densities across CRAFT, LFIS, PGPS, and our AF, with all methods sharing the same neural network architecture and training iterations. PGPS is tested without Langevin adjustments for fairness. Additional results, including LFIS with 256 time steps, CRAFT with 128 time steps, and PGPS with 128 time steps, are provided in Appendix D.

*Gaussian Mixture Models (GMMs):* Figure 3 shows the visualized sampling results of various methods on GMMs. Additionally, we tested unequally weighted GMMs, where two modes have double the weight of the others. Numerical evaluation metrics for experiments with different numbers of modes and dimensions are presented in Tables 2 and 3. Additional figures and results are provided in Appendix D.

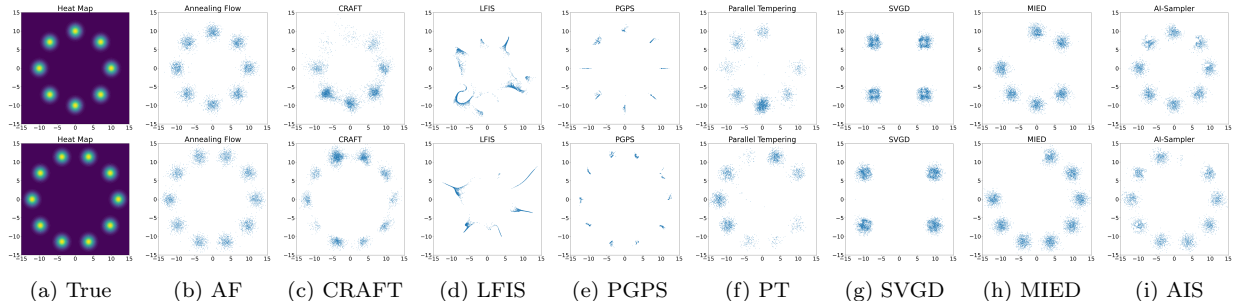


Figure 3: Sampling methods for Gaussian Mixture Models (GMM) with 8 and 10 modes arranged on circles with radii  $r = 10, 12$ . The number of time steps for CRAFT, LFIS, and PGPS is set to 10, the same as for AF.

*Truncated Normal Distribution:* Figure 7 in the Appendix shows the sampling results for the truncated normal distribution  $\tilde{q}(x) = 1_{\|x\| \geq c} \mathcal{N}(0, I_d)$ . Notably, even after relaxing  $1_{\|x\| > c}$  to  $1/(1 + \exp(-k(\|x\| - c)))$  in  $\nabla \log(1_{\|x\| \geq c} \mathcal{N}(0, I_d))$ , methods including LFIS, PGPS, SVGD, MIED, and AI-Sampler fail to produce meaningful results. There are also computational issues when implementing CRAFT for this task. Please refer to Figure 6 in Appendix D for the results of these algorithms.

*Funnel Distribution:* We tested each algorithm for the funnel distribution  $q(x_1, x_2, \dots, x_d) \propto \mathcal{N}(x_1 | 0, \sigma^2) \prod_{i=2}^d \mathcal{N}(x_i | 0, \exp(x_1))$  on the  $d = 5$  space. The Figure 9 in Appendix D shows the visualized sampling results projected onto a 3D space for the funnel distribution in a 5D space.

*Exp-Weighted Gaussian with an Extreme Number of Modes in High-Dimensional Spaces:*

We tested each algorithm on sampling from an extreme distribution:

$$p(x_1, x_2, \dots, x_{10}) \propto e^{10 \sum_{i=1}^{10} |x_i| - \frac{1}{2} \|x\|^2},$$

which has  $2^{10} = 1024$  modes arranged at the vertices of a 10-D cube. The L2-distance between two horizontally or vertically adjacent modes is 20, while the diagonal modes are separated by up to  $\sqrt{10 \cdot 20^2} \approx 63.25$ . We also tested on the extreme distribution:

$$p(x_1, x_2, \dots, x_{50}) \propto e^{10 \sum_{i=1}^{10} \frac{|x_i|}{\sigma_i^2} + 10 \sum_{i=11}^{50} \frac{x_i}{\sigma_i^2} - \frac{1}{2} \|x\|^2},$$

which has  $2^{10} = 1024$  modes arranged at the vertices of a 50-D space, with unequal variances across all modes along different dimensions.

Table 1: Number of Modes in a 50D Exponentially-Weighted Gaussian with 1024 Well-Separated Modes Explored by Different Methods. The number of time steps for AF, CRAFT, LFIS, and PGPS is set to 20.

	True	AF	CRAFT	LFIS	PGPS	PT	SVGD	MIED	AIS
$d = 2$	4	<b>4</b>	2.6	3.6	3.8	3.4	3.9	3.8	3.8
$d = 5$	32	<b>32</b>	22.3	27.4	31.2	25.2	28.5	28.0	28.3
$d = 10$	1024	<b>1024</b>	515.4	387.0	826.0	233.7	957.3	923.4	301.2
$d = 50$	1024	<b>1024</b>	473.2	298.2	813.6	< 10	916.4	890.6	125.6

Given the challenge of visualizing results in high-dimensional space, we first present the number of modes successfully explored by different algorithms across varying dimensions in Table 1. Each algorithm was run 10 times, with 20,000 points sampled per run, and the average number of modes explored was calculated. Additionally, Table 3 presents the Mode Weights Mean Squared Error, along with results of other distributions.

*Evaluation Metrics:* We report (1) the Maximum Mean Discrepancy (MMD), (2) the Wasserstein Distance, and (3) the Mode-Weight Mean Squared Error for each applicable experiment. The results for these metrics are presented in Tables 2 and 3. Appendix C.1 explains the details of these metrics. In the tables, GMM refers to Gaussian Mixture Models, while wGMM denotes unequally weighted Gaussian Mixture Models. The notation (w)GMM- $\{\text{number of modes}\}$ - $\{\text{radius of the circle}\}$  represents a (w)GMM with the specified number of modes arranged on a circle of the given radius. ExpGauss-1024 refers to exponentially weighted Gaussian experiments involving 1,024 widely separated modes. ExpGaussUV- $\{\text{number of UV dimensions}\}$ -1024 refers to ExpGauss with 1024 modes that have unequal variances across the specified number of dimensions, with  $\sigma_i^2 = 0.5$  for unequal variance dimensions and  $\sigma_i^2 = 1$  for others.

Table 2: MMD and Wasserstein Distance results:  $\cdot/\cdot$  represents MMD/Wasserstein.

Distributions \ Methods	AF	CRAFT	LFIS	PGPS	PT	SCGD	MIED	AI-Sampler
$d = 2$ GMM-6-8	$2.38 \times 10^{-3}/9.38 \times 10^{-1}$	<b><math>2.30 \times 10^{-3}/9.28 \times 10^{-1}</math></b>	$1.15 \times 10^{-2}/8.24 \times 10^{10}$	$7.12 \times 10^{-2}/6.33 \times 10^{10}$	$6.27 \times 10^{-2}/5.71 \times 10^{10}$	$9.35 \times 10^{-2}/9.97 \times 10^{10}$	$9.32 \times 10^{-3}/8.01 \times 10^{-1}$	<b><math>2.34 \times 10^{-3}/7.92 \times 10^{-1}</math></b>
$d = 2$ GMM-8-10	<b><math>2.45 \times 10^{-3}/7.22 \times 10^{-1}</math></b>	$8.98 \times 10^{-2}/7.57 \times 10^{10}$	$2.31 \times 10^{-2}/8.99 \times 10^{10}$	$6.32 \times 10^{-2}/5.82 \times 10^{10}$	$6.48 \times 10^{-2}/5.98 \times 10^{10}$	$1.51 \times 10^{-1}/1.14 \times 10^{11}$	$2.49 \times 10^{-2}/8.15 \times 10^{-1}$	<b><math>2.61 \times 10^{-3}/8.95 \times 10^{-1}</math></b>
$d = 2$ GMM-10-12	<b><math>3.01 \times 10^{-3}/8.05 \times 10^{-1}</math></b>	$9.06 \times 10^{-2}/8.73 \times 10^{10}$	$8.97 \times 10^{-2}/9.79 \times 10^{10}$	$7.01 \times 10^{-2}/6.09 \times 10^{10}$	$9.01 \times 10^{-2}/7.91 \times 10^{10}$	$1.85 \times 10^{-1}/1.82 \times 10^{11}$	$6.28 \times 10^{-2}/9.35 \times 10^{-1}$	$4.02 \times 10^{-3}/8.13 \times 10^{-1}$
$d = 2$ wGMM-10-12	<b><math>4.95 \times 10^{-3}/9.94 \times 10^{-1}</math></b>	$9.96 \times 10^{-2}/9.78 \times 10^{10}$	$1.14 \times 10^{-2}/1.02 \times 10^{11}$	$8.95 \times 10^{-2}/7.88 \times 10^{10}$	$7.02 \times 10^{-2}/6.48 \times 10^{10}$	$2.72 \times 10^{-1}/2.93 \times 10^{11}$	$8.31 \times 10^{-2}/1.06 \times 10^{10}$	$3.19 \times 10^{-3}/8.44 \times 10^{-1}$
$d = 5$ GMM-6-8	<b><math>5.82 \times 10^{-3}/1.97 \times 10^{10}</math></b>	$9.92 \times 10^{-2}/1.12 \times 10^{11}$	$1.23 \times 10^{-2}/1.01 \times 10^{11}$	$7.81 \times 10^{-2}/7.88 \times 10^{10}$	$8.83 \times 10^{-2}/1.07 \times 10^{11}$	$9.81 \times 10^{-2}/1.13 \times 10^{11}$	$8.01 \times 10^{-3}/2.52 \times 10^{10}$	$7.55 \times 10^{-2}/2.38 \times 10^{10}$
$d = 5$ GMM-8-10	<b><math>1.25 \times 10^{-3}/3.33 \times 10^{10}</math></b>	$9.76 \times 10^{-2}/1.98 \times 10^{11}$	$4.52 \times 10^{-2}/3.55 \times 10^{11}$	$7.76 \times 10^{-2}/8.21 \times 10^{10}$	$8.98 \times 10^{-2}/1.53 \times 10^{11}$	$9.63 \times 10^{-2}/2.07 \times 10^{11}$	$3.88 \times 10^{-2}/8.89 \times 10^{10}$	$5.26 \times 10^{-2}/5.53 \times 10^{10}$
$d = 5$ GMM-10-12	<b><math>1.57 \times 10^{-3}/2.82 \times 10^{10}</math></b>	$2.14 \times 10^{-1}/2.53 \times 10^{11}$	$7.25 \times 10^{-2}/4.89 \times 10^{11}$	$8.31 \times 10^{-2}/8.75 \times 10^{10}$	$1.18 \times 10^{-1}/1.83 \times 10^{11}$	$1.98 \times 10^{-1}/2.45 \times 10^{11}$	$9.88 \times 10^{-3}/7.89 \times 10^{10}$	$6.37 \times 10^{-3}/3.83 \times 10^{10}$
$d = 5$ wGMM-10-12	<b><math>4.31 \times 10^{-3}/3.53 \times 10^{10}</math></b>	$3.95 \times 10^{-1}/3.03 \times 10^{11}$	$8.38 \times 10^{-2}/5.21 \times 10^{11}$	$8.28 \times 10^{-2}/8.64 \times 10^{10}$	$1.05 \times 10^{-1}/2.13 \times 10^{11}$	$1.32 \times 10^{-1}/2.34 \times 10^{11}$	$2.03 \times 10^{-2}/1.13 \times 10^{11}$	$1.87 \times 10^{-2}/9.73 \times 10^{10}$

Table 3: Mode-Weight Mean Squared Error Across Distributions. The number of time steps for CRAFT, LFIS, and PGPS is set to 20, the same as for AF.

Distributions \ Methods	AF	CRAFT	LFIS	PGPS	SVGD	MIED	AI-Sampler
$d = 2$ GMM-6-8	$8.5 \times 10^{-5} \pm 3.7 \times 10^{-6}$	<b><math>7.7 \times 10^{-5} \pm 5.1 \times 10^{-6}</math></b>	$1.2 \times 10^{-4} \pm 2.8 \times 10^{-6}$	<b><math>7.4 \times 10^{-5} \pm 4.4 \times 10^{-6}</math></b>	$1.6 \times 10^{-2} \pm 8.4 \times 10^{-3}$	$1.4 \times 10^{-3} \pm 7.9 \times 10^{-4}$	<b><math>8.3 \times 10^{-5} \pm 4.8 \times 10^{-6}</math></b>
$d = 2$ GMM-8-10	<b><math>9.4 \times 10^{-5} \pm 1.2 \times 10^{-6}</math></b>	$2.7 \times 10^{-4} \pm 3.9 \times 10^{-5}$	$5.8 \times 10^{-4} \pm 8.2 \times 10^{-6}$	<b><math>9.8 \times 10^{-5} \pm 4.1 \times 10^{-6}</math></b>	$1.7 \times 10^{-2} \pm 9.2 \times 10^{-3}$	$1.5 \times 10^{-3} \pm 8.7 \times 10^{-4}$	$2.3 \times 10^{-4} \pm 5.2 \times 10^{-5}$
$d = 2$ GMM-10-12	<b><math>5.7 \times 10^{-5} \pm 7.6 \times 10^{-6}</math></b>	$2.6 \times 10^{-4} \pm 7.0 \times 10^{-5}$	$2.3 \times 10^{-3} \pm 4.1 \times 10^{-4}$	$2.2 \times 10^{-4} \pm 8.2 \times 10^{-5}$	$1.7 \times 10^{-2} \pm 8.2 \times 10^{-3}$	$5.6 \times 10^{-3} \pm 7.7 \times 10^{-4}$	$1.0 \times 10^{-3} \pm 6.8 \times 10^{-3}$
$d = 2$ wGMM-10-12	<b><math>9.5 \times 10^{-5} \pm 7.0 \times 10^{-6}</math></b>	<b><math>9.7 \times 10^{-5} \pm 9.8 \times 10^{-6}</math></b>	$3.8 \times 10^{-3} \pm 6.2 \times 10^{-4}$	$4.7 \times 10^{-4}/8.5 \times 10^{-5}$	$2.4 \times 10^{-2} \pm 9.3 \times 10^{-3}$	$5.2 \times 10^{-3} \pm 6.0 \times 10^{-4}$	$3.6 \times 10^{-3} \pm 6.0 \times 10^{-3}$
$d = 5$ GMM-6-8	<b><math>1.3 \times 10^{-4} \pm 4.8 \times 10^{-5}</math></b>	$1.5 \times 10^{-2} \pm 1.8 \times 10^{-3}$	$5.4 \times 10^{-4} \pm 1.3 \times 10^{-5}$	<b><math>1.2 \times 10^{-4} \pm 5.7 \times 10^{-5}</math></b>	$2.1 \times 10^{-2} \pm 7.5 \times 10^{-3}$	$1.1 \times 10^{-3} \pm 4.0 \times 10^{-4}$	$8.6 \times 10^{-3} \pm 2.1 \times 10^{-3}$
$d = 5$ GMM-8-10	<b><math>2.2 \times 10^{-4} \pm 2.9 \times 10^{-5}</math></b>	$1.1 \times 10^{-2} \pm 7.9 \times 10^{-3}$	$9.2 \times 10^{-4} \pm 4.1 \times 10^{-5}$	$4.8 \times 10^{-4} \pm 8.5 \times 10^{-5}$	$3.4 \times 10^{-2} \pm 7.5 \times 10^{-3}$	$4.8 \times 10^{-3} \pm 9.4 \times 10^{-4}$	$2.7 \times 10^{-3} \pm 6.5 \times 10^{-3}$
$d = 5$ GMM-10-12	<b><math>1.8 \times 10^{-4} \pm 6.5 \times 10^{-5}</math></b>	$8.8 \times 10^{-3} \pm 7.9 \times 10^{-4}$	$3.5 \times 10^{-3} \pm 4.9 \times 10^{-4}$	$5.2 \times 10^{-4} \pm 7.3 \times 10^{-5}$	$5.2 \times 10^{-2} \pm 1.8 \times 10^{-3}$	$3.1 \times 10^{-3} \pm 1.4 \times 10^{-4}$	$4.5 \times 10^{-3} \pm 8.0 \times 10^{-3}$
$d = 5$ wGMM-10-12	<b><math>7.3 \times 10^{-4} \pm 7.6 \times 10^{-5}</math></b>	$9.7 \times 10^{-3} \pm 2.9 \times 10^{-3}$	$7.6 \times 10^{-3} \pm 7.1 \times 10^{-4}$	$5.9 \times 10^{-4} \pm 7.8 \times 10^{-5}$	$6.4 \times 10^{-2} \pm 3.9 \times 10^{-3}$	$6.0 \times 10^{-3} \pm 6.5 \times 10^{-4}$	$7.9 \times 10^{-3} \pm 3.2 \times 10^{-3}$
$d = 10$ ExpGauss-1024	<b><math>5.3 \times 10^{-8} \pm 3.1 \times 10^{-9}</math></b>	$8.8 \times 10^{-7} \pm 3.5 \times 10^{-8}$	$1.5 \times 10^{-6} \pm 6.6 \times 10^{-7}$	$1.2 \times 10^{-7} \pm 3.5 \times 10^{-8}$	<b><math>5.5 \times 10^{-8} \pm 2.7 \times 10^{-9}</math></b>	$4.6 \times 10^{-6} \pm 1.8 \times 10^{-6}$	$8.6 \times 10^{-5} \pm 2.4 \times 10^{-6}$
$d = 50$ ExpGauss-1024	<b><math>9.8 \times 10^{-8} \pm 6.8 \times 10^{-9}</math></b>	$9.4 \times 10^{-7} \pm 8.0 \times 10^{-8}$	$2.2 \times 10^{-6} \pm 8.2 \times 10^{-7}$	$3.5 \times 10^{-7} \pm 8.0 \times 10^{-8}$	$3.3 \times 10^{-6} \pm 1.0 \times 10^{-6}$	$2.1 \times 10^{-6} \pm 9.2 \times 10^{-7}$	$1.1 \times 10^{-4} \pm 7.6 \times 10^{-5}$
$d = 50$ ExpGaussUV-2-1024	<b><math>8.6 \times 10^{-8} \pm 7.3 \times 10^{-9}</math></b>	$9.1 \times 10^{-7} \pm 7.9 \times 10^{-8}$	$7.1 \times 10^{-6} \pm 2.3 \times 10^{-7}$	$8.9 \times 10^{-7} \pm 6.4 \times 10^{-8}$	$7.6 \times 10^{-6} \pm 9.7 \times 10^{-7}$	$9.2 \times 10^{-6} \pm 1.1 \times 10^{-6}$	$1.7 \times 10^{-4} \pm 9.5 \times 10^{-5}$
$d = 50$ ExpGaussUV-10-1024	<b><math>8.8 \times 10^{-8} \pm 7.5 \times 10^{-9}</math></b>	$1.0 \times 10^{-6} \pm 9.8 \times 10^{-8}$	$9.0 \times 10^{-6} \pm 9.1 \times 10^{-7}$	$9.8 \times 10^{-7} \pm 8.4 \times 10^{-8}$	$1.1 \times 10^{-5} \pm 9.8 \times 10^{-7}$	$9.5 \times 10^{-6} \pm 1.9 \times 10^{-6}$	$1.4 \times 10^{-4} \pm 9.9 \times 10^{-5}$

*Bayesian Logistic Regression:* We use the same Bayesian logistic regression setting as in Liu & Wang (2016), where a hierarchical structure is assigned to the model parameters. The weights  $\beta$  follow a Gaussian prior  $p_0(\beta|\alpha) = N(\beta; 0, \alpha^{-1})$ , and  $\alpha$  follows a Gamma prior  $p_0(\alpha) = \text{Gamma}(\alpha; 1, 0.01)$ . Sampling is performed on the posterior  $p(\beta, \alpha|D)$ , where  $D = \{x_i, y_i\}_{i=1}^n$ . The performance comparisons are shown in Table 4. Detailed settings are given in C.4.

*Importance Flow:* Table 7 in the Appendix reports the preliminary results of the importance flow (discussed in Section 5) for estimating  $\mathbb{E}_{x \sim N(0, I)} [1_{\|x\| \geq c}]$  with varying radii  $c$  and dimensions. Please refer to C.5 for detailed experimental settings. Additionally, we discussed a possible extension of the Importance Flow framework in D.4.

Table 4: Bayesian Logistic Regression: comparison of different algorithms across datasets. In the table  $\cdot \pm \cdot / \cdot$  represents Accuracy( $\%$ ) $\pm$ std( $\%$ )/log-posterior. The number of time steps for AF is set to

Dataset \ Methods	AF	CRAFT	LFIS	PGPS	SVGD	MIED	AI-Sampler
Diabetes ( $d = 8$ )	<b>76.30 <math>\pm</math> 2.12 / -0.496</b>	76.20 $\pm$ 2.17 / -0.511	<b>76.22 <math>\pm</math> 2.95 / -0.499</b>	<b>76.32 <math>\pm</math> 2.17 / -0.495</b>	76.10 $\pm$ 2.5 / -0.502	75.80 $\pm$ 2.32 / -0.503	<b>76.30 <math>\pm</math> 2.18 / -0.493</b>
Breast Cancer ( $d = 10$ )	97.85 $\pm$ 1.12 / -0.017	<b>98.87 <math>\pm</math> 1.15 / -0.010</b>	96.37 $\pm$ 2.03 / -0.027	<b>98.86 <math>\pm</math> 1.10 / -0.010</b>	97.80 $\pm$ 2.54 / -0.023	<b>98.89 <math>\pm</math> 1.02 / -0.008</b>	97.83 $\pm$ 2.80 / -0.019
Heart ( $d = 13$ )	<b>88.46 <math>\pm</math> 2.73 / -0.316</b>	<b>88.43 <math>\pm</math> 2.98 / -0.318</b>	86.64 $\pm$ 3.55 / -0.427	87.22 $\pm$ 2.94 / -0.398	79.36 $\pm$ 3.78 / -0.588	86.70 $\pm$ 2.24 / -0.321	84.23 $\pm$ 2.54 / -0.458
Australian ( $d = 14$ )	<b>86.59 <math>\pm</math> 1.20 / -0.361</b>	85.03 $\pm$ 2.96 / -0.390	84.09 $\pm$ 1.98 / -0.357	85.37 $\pm$ 1.66 / -0.390	84.56 $\pm$ 2.87 / -0.365	85.17 $\pm$ 1.34 / -0.369	84.62 $\pm$ 2.30 / -0.375
Ijcnn1 ( $d = 22$ )	<b>91.96 <math>\pm</math> 0.05 / -0.195</b>	88.78 $\pm$ 0.12 / -0.225	89.84 $\pm$ 0.36 / -0.307	91.23 $\pm$ 1.29 / -0.201	89.44 $\pm$ 0.34 / -0.209	91.84 $\pm$ 0.15 / -0.198	88.32 $\pm$ 0.25 / -0.334
Svmguide3 ( $d = 22$ )	80.04 $\pm$ 0.95 / -0.468	78.56 $\pm$ 0.90 / -0.501	<b>80.33 <math>\pm</math> 1.15 / -0.475</b>	79.98 $\pm$ 0.99 / -0.487	78.89 $\pm$ 1.20 / -0.479	<b>80.56 <math>\pm</math> 1.04 / -0.468</b>	80.12 $\pm$ 0.98 / -0.472
German ( $d = 24$ )	<b>78.04 <math>\pm</math> 1.70 / -0.473</b>	77.54 $\pm$ 1.73 / -0.481	76.69 $\pm$ 2.34 / -0.485	77.72 $\pm$ 1.61 / -0.483	76.43 $\pm$ 1.70 / -0.483	77.21 $\pm$ 1.80 / -0.479	76.89 $\pm$ 1.84 / -0.484
Splice ( $d = 61$ )	<b>86.89 <math>\pm</math> 1.71 / -0.407</b>	81.09 $\pm$ 2.23 / -0.494	81.96 $\pm$ 1.34 / -0.475	82.78 $\pm$ 2.07 / -0.471	82.45 $\pm$ 1.97 / -0.473	83.10 $\pm$ 1.53 / -0.458	80.08 $\pm$ 1.90 / -0.499
Codon Usage ( $d = 70$ )	<b>98.47 <math>\pm</math> 0.39 / -0.013</b>	93.54 $\pm$ 1.10 / -0.198	96.37 $\pm$ 0.86 / -0.086	95.28 $\pm$ 1.62 / -0.101	93.27 $\pm$ 1.95 / -0.202	94.05 $\pm$ 1.88 / -0.192	90.55 $\pm$ 2.31 / -0.275

*Significance of Annealing Procedures:* We comment that annealing procedures play a crucial role in the success of our AF in high-dimensional settings with widely separated modes. Appendix D.3.2 presents ablation studies for cases with no or very few annealing steps. This unique feature allows AF to succeed on challenging distributions, unlike most NFs used for sampling.

*Minimal Dependence on MC Assistance:* AF depends on the choice of annealing steps, while CRAFT, LFIS, and PGPS can also be adapted to rely on annealing. However, CRAFT heavily depends on the choice of the MC kernel, which is one of the major functioning components of the algorithm. LFIS heavily depends on accurate score estimation for training, necessitating significantly more time steps. PGPS relies heavily on Langevin adjustments after each step, without which its performance becomes poor. In contrast, AF requires minimal assistance to succeed.

*Computational Efficiency:* In Tables 8 and 9 of Appendix D, we present the training and sampling times for AF, CRAFT, LFIS, and PGPS. In particular, AF requires only 1/10 the intermediate time steps of LFIS and 1/5 of CRAFT and PGPS to achieve superior results in our experiments. We also provide ablation studies in D.3.2 with even fewer time steps. In addition, in our experiments, AF with a single 32-unit hidden layer and sigmoid activation is sufficient for almost all tasks except Exp-weighted Gaussian, which requires only 32-32 hidden layers. In contrast, as stated in the official implementations, LFIS and PGPS require 64-64 or 128-128 hidden layers.

*Training Stability:* Our unique dynamic optimal transport (OT) objective with  $W_2$  regularization is key to ensuring much more stable performance, even with far fewer intermediate time steps, compared to methods CRAFT, LFIS, and PGPS. In Appendix D.3, we provide ablation studies on AF, CRAFT, LFIS, and PGPS, demonstrating their performance with even fewer intermediate time steps. Unlike the score-matching training, the unique dynamic OT objective of AF is crucial for ensuring stability, achieving much higher efficiency, and enabling successful sampling in high-dimensional and multi-modal settings.

## 7 Discussions

In this paper, we have proposed the Annealing Flow (AF) algorithm, a novel and flexible approach for sampling from high-dimensional and multi-modal distributions. With the unique Annealing-guided dynamic optimal transport objective, AF offers numerous advantages over existing methods, including superior performance on extreme distributions, significantly enhanced training efficiency compared to other NF methods, minimal reliance on MC assistance, and enhanced training stability compared to other NF methods.

We establish in Proposition 4 that the infinitesimal optimal velocity field corresponds to the score difference between consecutive annealing densities. This distinguishes our dynamic OT-based objective from recent Annealing-like methods (Fan et al.; Tian et al., 2024). In Appendix B, we demonstrate the equivalence of AF’s objective to the Wasserstein Gradient Flow and its associated convergence theorems. Extensive experiments demonstrate that AF performs well across a variety of challenging distributions and real-world datasets. Finally, the importance flow discussed in Section 5 may be extended to a distribution-free model, allowing one to learn an importance flow from a dataset for sampling its Least-Favorable Distribution (LFD) with minimal variance, as further discussed in D.4.

# A Proofs

## A.1 Proofs in Section 3.2

**Proposition 1.** (KL-Divergence Decomposition) *Given the unnormalized density  $f_{k-1}$ , the KL-Divergence between  $\mathcal{T}_{\#}f_{k-1}$  and  $f_k$  is equivalent to:*

$$KL(\mathcal{T}_{\#}f_{k-1} \| f_k) = c + \mathbb{E}_{x \sim f_{k-1}} \left[ \tilde{E}_k(x(t_k)) - \int_{t_{k-1}}^{t_k} \nabla \cdot \mathbf{v}_{\mathbf{k}}(x(s), s) ds \right],$$

up to a constant  $c$  that is independent of  $\mathbf{v}_{\mathbf{k}}(x(s), s)$ .

*Proof:*

Let  $\rho(x, t)$  denote the density evolution under the transport map  $\mathcal{T}$ , as defined in (2). By the constraint (2) in the transport map objective (3), we have  $\mathcal{T}_{\#}f_{k-1}(x) = \rho(x, t_k)$ . The expression for KL-divergence is given by:

$$KL(\mathcal{T}_{\#}f_{k-1} \| f_k) = \mathbb{E}_{x \sim \rho(x, t_k)} \left[ \log \frac{\mathcal{T}_{\#}f_{k-1}(x)}{f_k(x)} \right] = \mathbb{E}_{x \sim \rho(x, t_k)} [\log \mathcal{T}_{\#}f_{k-1}(x) - \log f_k(x)].$$

Now, recall that  $-\log \tilde{f}_k(x) = \tilde{E}_k(x)$ , so we substitute:

$$\begin{aligned} KL(\mathcal{T}_{\#}f_{k-1} \| f_k) &= \mathbb{E}_{x \sim \rho(x, t_k)} \left[ \log \mathcal{T}_{\#}f_{k-1}(x) + \tilde{E}_k(x) \right] - \log Z_k \\ &= \mathbb{E}_{x \sim \rho(x, t_{k-1})} \left[ \log \mathcal{T}_{\#}f_{k-1}(x(t_k)) + \tilde{E}_k(x(t_k)) \right] - \log Z_k, \end{aligned}$$

where the second equality holds under the constraints (1) and (2). The density  $\rho$  evolves according to (2), and equivalently, the particles  $x(t)$  evolve according to (1).

Next, to compute  $\log \mathcal{T}_{\#}f_{k-1}(x(t_k))$ , we use the fact that the dynamics of the pushforward density  $\rho$  are governed by the velocity field  $\mathbf{v}_{\mathbf{k}}(x(s), s)$ :

$$\begin{aligned} \frac{d}{ds} \log \rho(x(s), s) &= \frac{\nabla \rho(x(s), s) \cdot \partial_s x(s) + \partial_s \rho(x(s), s)}{\rho(x(s), s)} \\ &= \frac{\nabla \rho \cdot \mathbf{v}_{\mathbf{k}} - \nabla \cdot (\rho \mathbf{v}_{\mathbf{k}})}{\rho} \Big|_{(x(s), s)} \quad (\text{by (1) and (2)}) \\ &= \frac{\nabla \rho \cdot \mathbf{v}_{\mathbf{k}} - (\nabla \rho \cdot \mathbf{v}_{\mathbf{k}} + \rho \nabla \cdot \mathbf{v}_{\mathbf{k}})}{\rho} \Big|_{(x(s), s)} \\ &= -\nabla \cdot \mathbf{v}_{\mathbf{k}}(x(s), s). \end{aligned}$$

Integrating this equation over the interval  $s \in [t_{k-1}, t_k]$ , we find:

$$\log \mathcal{T}_{\#}f_{k-1}(x(t_k)) = \log \rho(x(t_k), t_k) = \log \rho(x(t_{k-1}), t_{k-1}) - \int_{t_{k-1}}^{t_k} \nabla \cdot \mathbf{v}_{\mathbf{k}}(x(s), s) ds.$$

We now substitute this result back into the KL-divergence expression:

$$KL(\mathcal{T}_{\#}f_{k-1} \| f_k) = \mathbb{E}_{x \sim \rho(x, t_{k-1})} \left[ \log \rho(x(t_{k-1}), t_{k-1}) - \int_{t_{k-1}}^{t_k} \nabla \cdot \mathbf{v}_{\mathbf{k}}(x(s), s) ds + \tilde{E}_k(x(t_k)) \right] - \log Z_k.$$

Note that  $\mathbb{E}_{x \sim \rho(x(t_{k-1}), t_{k-1})} [\log \rho(x(t_{k-1}), t_{k-1})]$  is independent of  $\mathbf{v}_{\mathbf{k}}(x(s), s)$  and thus acts as a constant term, along with  $-\log Z_k$ , which we now denote as  $c$ . After successfully training the previous velocity fields, we have  $\rho(x, t_{k-1}) = f_{k-1}(x)$ . Therefore, the relevant terms for the KL-divergence are:

$$KL(\mathcal{T}_{\#}f_{k-1} \| f_k) = c + \mathbb{E}_{x \sim f_{k-1}} \left[ \tilde{E}_k(x(t_k)) - \int_{t_{k-1}}^{t_k} \nabla \cdot \mathbf{v}_{\mathbf{k}}(x(s), s) ds \right].$$

**Proposition 2.** (Wasserstein Distance Discretization) *Let  $x(t)$  be particle trajectories driven by a smooth velocity field  $\mathbf{v}_{\mathbf{k}}(x(t), t)$  over the time interval  $[t_{k-1}, t_k]$ , where  $h_k = t_k - t_{k-1}$ . Assume that  $\mathbf{v}_{\mathbf{k}}(x, t)$  is Lipschitz continuous in both  $x$  and  $t$ . By dividing  $[t_{k-1}, t_k]$  into  $S$  equal mini-intervals with grid points  $t_{k-1,s}$  (where  $s = 0, 1, \dots, S$  and  $t_{k-1,0} = t_{k-1}$ ,  $t_{k-1,S} = t_k$ ), the following approximation holds:*

$$\int_{t_{k-1}}^{t_k} \mathbb{E}_{x(t)} [\|\mathbf{v}_{\mathbf{k}}(x(t), t)\|^2] dt = \frac{S}{h_k} \sum_{s=0}^{S-1} \mathbb{E} [\|x(t_{k-1,s+1}) - x(t_{k-1,s})\|^2] + O(h_k^2/S).$$

As  $h_k \rightarrow 0$  or  $S \rightarrow \infty$ , the error term  $O(h_k^2/S)$  becomes negligible.

*Proof:*

Consider particle trajectories  $x(t)$  driven by a sufficiently smooth velocity field  $\mathbf{v}_{\mathbf{k}}(x(t), t)$  over the time interval  $[t_{k-1}, t_k]$ , where  $h_k = t_k - t_{k-1}$ . We divide this interval into  $S$  equal mini-intervals of length  $\delta t = \frac{h_k}{S}$ , resulting in grid points  $t_{k-1,s} = t_{k-1} + s\delta t$  for  $s = 0, 1, \dots, S$ , where  $\delta t = \frac{t_k - t_{k-1}}{S}$ .

Within each mini-interval  $[t_{k-1,s}, t_{k-1,s+1}]$ , we perform a Taylor expansion of  $x(t)$  around  $t_{k-1,s}$ :

$$x(t_{k-1,s+1}) = x(t_{k-1,s}) + \mathbf{v}_{\mathbf{k}}(x(t_{k-1,s}), t_{k-1,s})\delta t + \frac{1}{2} \frac{d\mathbf{v}_{\mathbf{k}}}{dt} \delta t^2 + O(\delta t^3),$$

where  $\frac{d\mathbf{v}_{\mathbf{k}}}{dt}$  denotes the total derivative of  $\mathbf{v}_{\mathbf{k}}$  with respect to time.

The squared displacement over the mini-interval  $[t_{k-1,s}, t_{k-1,s+1}]$  is given by:

$$\begin{aligned} \|x(t_{k-1,s+1}) - x(t_{k-1,s})\|^2 &= \left\| \mathbf{v}_{\mathbf{k}}(x(t_{k-1,s}), t_{k-1,s})\delta t + \frac{1}{2} \frac{d\mathbf{v}_{\mathbf{k}}}{dt} \delta t^2 + O(\delta t^3) \right\|^2 \\ &= \|\mathbf{v}_{\mathbf{k}}(x(t_{k-1,s}), t_{k-1,s})\|^2 \delta t^2 + O(\delta t^3), \end{aligned}$$

as we assume that  $\mathbf{v}_{\mathbf{k}}$  is  $L$ -Lipschitz continuous and it follows that  $|\frac{d\mathbf{v}_{\mathbf{k}}}{dt}| \leq L$ . The higher-order terms  $O(\delta t^3)$  become negligible as  $\delta t \rightarrow 0$ .

Summing the expected squared displacements over all mini-intervals, we obtain:

$$\sum_{s=0}^{S-1} \mathbb{E} [\|x(t_{k-1,s+1}) - x(t_{k-1,s})\|^2] = \delta t^2 \sum_{s=0}^{S-1} \mathbb{E} [\|\mathbf{v}_{\mathbf{k}}(x(t_{k-1,s}), t_{k-1,s})\|^2] + O(S \cdot \delta t^3).$$

Now, we examine the L.H.S. of Proposition 2 by approximating the integral of the expected squared velocity using a Riemann sum:

$$\begin{aligned} \int_{t_{k-1}}^{t_k} \mathbb{E}_{x(t)} [\|\mathbf{v}_{\mathbf{k}}(x(t), t)\|^2] dt &= \delta t \sum_{s=0}^{S-1} \mathbb{E} [\|\mathbf{v}_{\mathbf{k}}(x(t_{k-1,s}), t_{k-1,s})\|^2] + O(S \cdot \delta t^2) \\ &= \delta t \left[ \frac{1}{\delta t^2} \sum_{s=0}^{S-1} \mathbb{E} [\|x(t_{k-1,s+1}) - x(t_{k-1,s})\|^2] + O(S \cdot \delta t) \right] + O(S \cdot \delta t^2) \\ &= \frac{1}{\delta t} \sum_{s=0}^{S-1} \mathbb{E} [\|x(t_{k-1,s+1}) - x(t_{k-1,s})\|^2] + O(S \cdot \delta t^2), \end{aligned}$$

where the Riemann sum error term  $O(S \cdot \delta t^2)$  arises from a well-known result (for instance, see Chapter 1 of Axler (2020)), given the assumption that  $\mathbf{v}_{\mathbf{k}}$  is  $L$ -Lipschitz continuous.



## A.2 Proofs in Section 3.3

**Proposition 3.** (Objective Reformulation) *Denote  $h_k = t_k - t_{k-1}$ , and let  $\mathbf{s}_k = \nabla \log f_k(x)$  denote the score function of  $f_k$ . As  $h_k \rightarrow 0$  and with  $\gamma = \frac{1}{2}$ , the objective in (10) becomes equivalent to the following:*

$$\min_{\mathbf{v}_k = \mathbf{v}_k(\cdot, 0)} \mathbb{E}_{x \sim f_{k-1}} \left[ -T_{f_k} \mathbf{v}_k + \frac{1}{2} \|\mathbf{v}_k\|^2 \right], \quad T_{f_k} \mathbf{v}_k := \mathbf{s}_k \cdot \mathbf{v}_k + \nabla \cdot \mathbf{v}_k.$$

*Proof:*

From the Neural ODE (1) and using Taylor's expansion, we obtain:

$$x(t_k) - x(t_{k-1}) = \int_{t_{k-1}}^{t_k} \mathbf{v}_k(x(s), s) ds = h_k \mathbf{v}_k(x(t_{k-1}), t_{k-1}) + O(h_k^2)$$

Next, by performing Taylor expansion of  $\tilde{E}_k(x(t_k))$  around  $t_{k-1}$ :

$$\begin{aligned} \tilde{E}_k(x(t_k)) &= \tilde{E}_k(x(t_{k-1})) + (x(t_k) - x(t_{k-1})) \nabla \tilde{E}_k(x(t_{k-1})) + O(h_k^2) \\ &= \tilde{E}_k(x(t_{k-1})) + h_k \nabla \tilde{E}_k(x(t_{k-1})) \cdot \mathbf{v}_k(x(t_{k-1}), t_{k-1}) + O(h_k^2) \end{aligned}$$

Besides, we also have that:

$$\int_{t_{k-1}}^{t_k} \nabla \cdot \mathbf{v}_k(x(s), s) ds = h_k \nabla \cdot \mathbf{v}_k(x(t_{k-1}), t_{k-1}) + O(h_k^2).$$

As  $h_k \rightarrow 0$ , we no longer need to divide the time interval, i.e.,  $S = 1$ . By defining the score function as  $\mathbf{s}_k = \nabla \log f_k = -\nabla \tilde{E}_k$ , the objective function (10) can be then approximated as:

$$\begin{aligned} &\mathbb{E}_{x \sim f_{k-1}} \left[ \tilde{E}_k(x(t_k)) - \int_{t_{k-1}}^{t_k} \nabla \cdot \mathbf{v}_k(x(s), s) ds + \frac{1}{2h_k} \|x(t_k) - x(t_{k-1})\|^2 \right] \\ &= \mathbb{E}_{x \sim f_{k-1}} \left[ \left( \tilde{E}_k(x(t_{k-1})) - h_k \mathbf{s}_k(x(t_{k-1})) \cdot \mathbf{v}_k(x(t_{k-1}), t_{k-1}) + O(h_k^2) \right) \right. \\ &\quad \left. - \left( h_k \nabla \cdot \mathbf{v}_k(x(t_{k-1}), t_{k-1}) + O(h_k^2) \right) + \frac{1}{2h_k} \|h_k \mathbf{v}_k(x(t_{k-1})) + O(h_k^2)\|^2 \right] \\ &= \mathbb{E}_{x \sim f_{k-1}} \left[ \tilde{E}_k(x) + h_k \left( -\mathbf{s}_k(x) \cdot \mathbf{v}_k(x, t_{k-1}) - \nabla \cdot \mathbf{v}_k(x, t_{k-1}) + \frac{1}{2} \|\mathbf{v}_k(x, t_{k-1})\|^2 \right) + O(h_k^2) \right] \end{aligned}$$

Since  $\mathbb{E}_{x(t_{k-1}) \sim f_{k-1}} [\tilde{E}_k(x(t_{k-1}))]$  is independent of  $\mathbf{v}_k(x, t)$ , as  $h_k \rightarrow 0$ , the minimization of the leading term is equivalent to:

$$\min_{\mathbf{v}_k = \mathbf{v}_k(\cdot, 0)} \mathbb{E}_{x \sim f_{k-1}} \left[ -T_{f_k} \mathbf{v}_k + \frac{1}{2} \|\mathbf{v}_k\|^2 \right], \quad T_{f_k} \mathbf{v}_k := \mathbf{s}_k \cdot \mathbf{v}_k + \nabla \cdot \mathbf{v}_k.$$

**Proposition 4:** (Optimal Velocity Field as Score Difference) *Suppose  $h_k \rightarrow 0$ . Let  $f_{k-1}$  and  $f_k$  be continuously differentiable on  $\mathbb{R}^d$ . Assume that  $\nabla \cdot \mathbf{v}_k(x)$  exists for all  $x \in \mathbb{R}^d$ , and  $\nabla \cdot \mathbf{v}_k(x)$ ,  $\mathbf{s}_{k-1}$  and  $\mathbf{s}_k$  belong to  $L^2(f_{k-1})$ . Assume that the components of  $\mathbf{v}_k$  are independent and  $\lim_{\|x\| \rightarrow \infty} f_{k-1}(x) \|\mathbf{v}_k(x)\|_2 = 0$ . Under these conditions, the minimizer of (10) is:*

$$\mathbf{v}_k^* = \mathbf{s}_k - \mathbf{s}_{k-1}.$$

*Proof:*

Under the assumptions that  $h_k \rightarrow 0$  and  $\gamma = \frac{1}{2}$ , we begin by considering the equivalent minimization objective derived in Proposition 3:

$$\min_{\mathbf{v}_k} J(\mathbf{v}_k) := \min_{\mathbf{v}_k} \mathbb{E}_{x \sim f_{k-1}} \left[ -T_{f_k} \mathbf{v}_k + \frac{1}{2} \|\mathbf{v}_k\|^2 \right], \quad T_{f_k} \mathbf{v}_k := \mathbf{s}_k \cdot \mathbf{v}_k + \nabla \cdot \mathbf{v}_k.$$

Expanding the objective functional, we have:

$$\mathbb{E}_{x \sim f_{k-1}} \left[ -\mathbf{s}_{\mathbf{k}} \cdot \mathbf{v}_{\mathbf{k}} - \nabla \cdot \mathbf{v}_{\mathbf{k}} + \frac{1}{2} \|\mathbf{v}_{\mathbf{k}}\|^2 \right] = \int_{\mathbb{R}^d} f_{k-1}(x) \left( -\mathbf{s}_{\mathbf{k}}(x) \cdot \mathbf{v}_{\mathbf{k}}(x) - \nabla \cdot \mathbf{v}_{\mathbf{k}}(x) + \frac{1}{2} \|\mathbf{v}_{\mathbf{k}}(x)\|^2 \right) dx.$$

Define  $B_r = \{x \in \mathbb{R}^d : \|x\| \leq r\}$ , and let  $\partial B_r$  denote the boundary of  $B_r$ , which is the sphere of radius  $r$ . Under the assumption that  $\lim_{\|x\| \rightarrow \infty} f_{k-1}(x) \|\mathbf{v}_{\mathbf{k}}(x)\|_2 = 0$ , we have the following:

$$\begin{aligned} \left| \int_{\mathbb{R}^d} \nabla \cdot (f_{k-1} \mathbf{v}_{\mathbf{k}}) dx \right| &= \lim_{r \rightarrow \infty} \left| \int_{B_r} \nabla \cdot (f_{k-1} \mathbf{v}_{\mathbf{k}}) dx \right| \\ &= \lim_{r \rightarrow \infty} \left| \int_{\partial\{x \in \mathbb{R}^d : \|x\| < r\}} f_{k-1}(x) \mathbf{v}_{\mathbf{k}}(x) \cdot \mathbf{n}(x) dS(x) \right| \\ &\leq \lim_{r \rightarrow \infty} \int_{\partial\{x \in \mathbb{R}^d : \|x\| < r\}} f_{k-1} \|\mathbf{v}_{\mathbf{k}}\|_2 \|\mathbf{n}_{\mathbf{k}}\|_2 dS(x) \\ &= \lim_{r \rightarrow \infty} \int_{\partial\{x \in \mathbb{R}^d : \|x\| < r\}} f_{k-1} \|\mathbf{v}_{\mathbf{k}}\|_2 dS(x) \\ &= 0 \end{aligned}$$

Therefore,  $\int_{\mathbb{R}^d} \nabla \cdot (f_{k-1} \mathbf{v}_{\mathbf{k}}) dx = 0$ . Next, we further expand the divergence theorem:

$$\begin{aligned} 0 &= \int_{\mathbb{R}^d} \nabla \cdot (f_{k-1}(x) \mathbf{v}_{\mathbf{k}}(x)) dx \\ &= \int_{\mathbb{R}^d} f_{k-1}(x) \nabla \cdot \mathbf{v}_{\mathbf{k}}(x) dx + \int_{\mathbb{R}^d} \mathbf{v}_{\mathbf{k}}(x) \cdot \nabla f_{k-1}(x) dx \\ &= \int_{\mathbb{R}^d} f_{k-1}(x) \nabla \cdot \mathbf{v}_{\mathbf{k}}(x) dx + \int_{\mathbb{R}^d} \mathbf{v}_{\mathbf{k}}(x) \cdot \mathbf{s}_{\mathbf{k}-1}(x) f_{k-1}(x) dx \end{aligned}$$

Substitute the result back into the objective functional, we have:

$$\begin{aligned} \mathbb{E}_{x \sim f_{k-1}} \left[ -\mathbf{s}_{\mathbf{k}} \cdot \mathbf{v}_{\mathbf{k}} - \nabla \cdot \mathbf{v}_{\mathbf{k}} + \frac{1}{2} \|\mathbf{v}_{\mathbf{k}}\|^2 \right] &= \int_{\mathbb{R}^d} f_{k-1}(x) \left( -\mathbf{s}_{\mathbf{k}}(x) \cdot \mathbf{v}_{\mathbf{k}}(x) - \nabla \cdot \mathbf{v}_{\mathbf{k}}(x) + \frac{1}{2} \|\mathbf{v}_{\mathbf{k}}(x)\|^2 \right) dx \\ &= \int_{\mathbb{R}^d} f_{k-1}(x) \left( (\mathbf{s}_{\mathbf{k}-1}(x) - \mathbf{s}_{\mathbf{k}}(x)) \cdot \mathbf{v}_{\mathbf{k}}(x) + \frac{1}{2} \|\mathbf{v}_{\mathbf{k}}(x)\|^2 \right) dx. \end{aligned}$$

The integrand does not involve  $\nabla v_{k,j}(x)$ ,  $j = 1, \dots, d$  and higher-order derivatives. Assuming the components  $v_{k,j}$ ,  $j = 1, \dots, d$  of  $\mathbf{v}_{\mathbf{k}}$  are independent, we can take the functional derivative component-wise and set them to zero:

$$\frac{\delta J}{\delta \mathbf{v}_{\mathbf{k}}} = f_{k-1} (\mathbf{v}_{\mathbf{k}} + (\mathbf{s}_{\mathbf{k}-1} - \mathbf{s}_{\mathbf{k}})) = 0,$$

Since  $f_{k-1} > 0$  for all  $x$ , this implies:

$$\mathbf{v}_{\mathbf{k}}^* = \mathbf{s}_{\mathbf{k}} - \mathbf{s}_{\mathbf{k}-1}.$$

### A.3 Proofs in Section 5.2

**Density Ratio Estimation (DRE)** *By optimizing the following loss function:*

$$\mathcal{L}_k(\theta_k) = \mathbb{E}_{x(t_{k-1}) \sim f_{k-1}} \left[ \log(1 + e^{-r_k(x_i(t_{k-1}))}) \right] + \mathbb{E}_{x(t_k) \sim f_k} \left[ \log(1 + e^{r_k(x_i(t_k))}) \right],$$

the model learns an optimal  $r^*(x; \theta_k) = \log \frac{f_{k-1}(x)}{f_k(x)}$ .

*Proof:*

Express the loss function as integrals over  $x$ :

$$\mathcal{L}_k = \int f_{k-1}(x) \log(1 + e^{-r_k(x)}) dx + \int f_k(x) \log(1 + e^{r_k(x)}) dx.$$

Compute the functional derivative of  $\mathcal{L}_k$  with respect to  $r_k$ :

$$\frac{\delta \mathcal{L}_k(r_k)}{\delta r_k} = -f_{k-1}(x) \cdot \frac{e^{-r_k(x)}}{1 + e^{-r_k(x)}} + f_k(x) \cdot \frac{e^{r_k(x)}}{1 + e^{r_k(x)}}.$$

Next, we can set the derivative  $\delta l_k / \delta r_k(x)$  to zero to find the minimizer  $r_k^*(x)$ :

$$r_k^*(x) = \ln \left( \frac{f_{k-1}(x)}{f_k(x)} \right).$$

Therefore, by concatenating each  $r_k^*(x)$ , we obtain

$$r^*(x) = \sum_{k=1}^K r_k^*(x) = \log \frac{f_{K-1}(x)}{f_K(x)} \cdot \frac{f_{K-2}(x)}{f_{K-1}(x)} \cdots \frac{f_0(x)}{f_1(x)} = \log \frac{f_0(x)}{f_K(x)} = \log \frac{\pi_0(x)}{q^*(x)},$$

the log density ratio between  $\pi_0(x)$  and  $q^*(x)$ .

## B Equivalence to Wasserstein gradient flow when $\beta = 1$

In this section, we demonstrate the equivalence between the dynamic optimal transport (OT) objective of AF and the Wasserstein Gradient Flow, under the condition that all  $\beta_k$  ( $k = 1, 2, \dots, K$ ) are set to 1, and a static Wasserstein regularization is used in place of the dynamic Wasserstein regularization introduced in 9.

*Langevin Dynamics and Fokker-Planck Equation:* Langevin Dynamics is represented by the following SDE.

$$dX_t = -\nabla E(X_t) dt + \sqrt{2} dW_t, \quad (16)$$

where  $E(x)$  is the energy function of the equilibrium density  $f(x, T) = q(x)$ . Let  $X_0 \sim p_X$  and denote the density of  $X_t$  by  $\rho(x, t)$ . The Langevin Dynamics corresponds to the Fokker-Planck Equation (FPE), which describes the evolution of  $\rho(x, t)$  towards the equilibrium  $\rho(x, T) = q(x)$ , as follows:

$$\partial_t \rho = \nabla \cdot (\rho \nabla E + \nabla \rho), \quad \rho(x, 0) = p_X(x). \quad (17)$$

*JKO Scheme and Wasserstein Gradient Flow:* The Jordan-Kinderlehrer-Otto (JKO) scheme (Jordan et al., 1998) is a time discretization scheme for gradient flows to minimize  $\text{KL}(\rho||q)$  under the Wasserstein-2 metric. Given a target density  $q$  and a functional  $\mathcal{F}(\rho, q) = \text{KL}(\rho||q)$ , the JKO scheme approximates the continuous gradient flow of  $\rho(x, t)$  by solving a sequence of minimization problems. Assume there are  $K$  steps with time stamps  $0 = t_0, t_1, \dots, t_K = T$ , at each time stamp  $t_k$ , the scheme updates  $\rho_k$  at each time step by minimizing the functional

$$\rho_k = \arg \min_{\rho} \left( \mathcal{F}(\rho, q) + \frac{1}{2\tau} W_2^2(\rho, \rho_{k-1}) \right), \quad (18)$$

where  $W_2(\rho, \rho_{k-1})$  denotes the squared 2-Wasserstein distance between the probability measures  $\rho$  and  $\rho_k$ . It was proven in Jordan et al. (1998) that as  $h = t_k - t_{k-1}$  approaches 0, the solution  $\rho(\cdot, kh)$  provided by the JKO scheme converges to the solution of (17), at each step  $k$ .

It is straightforward to see that solving for the transport density  $\rho_k$  using (18) is equivalent to solving for the transport map  $\mathcal{T}_k$  via:

$$\mathcal{T}_k = \arg \min_{\mathcal{T}: \mathbb{R}^d \rightarrow \mathbb{R}^d} \left( \text{KL}(\mathcal{T}_{\#} \rho_{k-1} || q) + \frac{1}{2\tau} \mathbb{E}_{x \sim \rho_{k-1}} \|x - \mathcal{T}_k(x)\|^2 \right) \quad (19)$$

Therefore, it is immediately evident that the Wasserstein gradient flow based on the discretized JKO scheme is equivalent to (6) when each  $\tilde{f}_k(x)$  is set as the target distribution  $q(x)$ , i.e., when all  $\beta_k$  are set to 1, and the second term in the objective (6) is relaxed to a static  $W_2$  regularization instead of a dynamic  $W_2$  regularization.

There are some well-established properties regarding the convergence of densities under the Wasserstein Gradient Flow objective when the target distribution  $q(x)$  is log-concave. Define  $\mathcal{P}_2 = \{P : \int_{\mathbb{R}^d} \|x\|^2 dP(x) < \infty\}$  and  $\mathcal{P}_2^* = \{P \in \mathcal{P}_2 : P \ll dx\}$ .

**Assumption 1** For all  $n$ , the learned velocity field  $\hat{v}_n$  guarantees that the mappings  $T_n$  is non-degenerate. Additionally, for the time interval  $[t_{n-1}, t_n]$ , the integrated squared deviation of the velocity field satisfies the inequality

$$\int_{t_{n-1}}^{t_n} \int_{\mathbb{R}^d} \|v - \hat{v}\|^2 \rho \, dx \, dt \leq \epsilon^2, \quad \epsilon \in (0, 1).$$

**Assumption 2**  $F(\rho, q) : \rho \rightarrow (-\infty, \infty]$  where  $\int_{\mathbb{R}^d} \|x\|^2 d\rho(x) < \infty$ , is lower semi-continuous;  $\text{Dom}(F) \subset \mathcal{P}_2^f$ ;  $F(\rho, q)$  is  $\lambda$ -convex a.g.g. in  $\mathcal{P}_2 = \{P : \int_{\mathbb{R}^d} \|x\|^2 dP(x) < \infty\}$ .

When the energy function  $E$  of  $q = e^{-E}$  is strongly convex, and  $F(\rho, q)$  is chosen as in (19) in our method, Assumption 2 holds true. Under the Assumptions 1-2, the Wasserstein Gradient Flow exhibits a polynomial convergence property in terms of  $W_2$ -distance:

**Theorem 1** (Cheng et al. (2023), Thm 4.3) Assume  $q \in \mathcal{P}_2$  is the global minimum of  $G$ , and that the Assumptions 1-2 hold, with  $\lambda \in (0, 1]$  and  $0 < \tau < 2$ . Then, for  $n = 1, 2, \dots$ , the following inequality is satisfied:

$$W_2^2(p_n, q) \leq \left(1 + \frac{\tau\lambda}{2}\right)^{-n} W_2^2(p_0, q) + \frac{4\epsilon^2}{\lambda^2}.$$

In particular, if

$$n \geq \frac{8}{\tau\lambda} \left( \log W_2(p_0, q) + \log \frac{\lambda}{\epsilon} \right),$$

then:

$$W_2(p_n, q) \leq \sqrt{\frac{5\epsilon^2}{\lambda^2}}, \quad G(p_{n+1}) - G(q) \leq \frac{9}{2\tau} \left(\frac{\epsilon}{\lambda}\right)^2.$$

**Assumption 3** There exist positive constants  $C_1, C_2, L$  such that, for all  $n$ , on the time interval  $[t_{n-1}, t_n]$ , which can be shifted to  $[0, \gamma]$ :

- (A1) For any  $t \in [0, \gamma]$ , the functions  $\rho_t$  and  $\hat{\rho}_t$  are positive on  $\mathbb{R}^d$ , and  $\rho_t(x), \hat{\rho}_t(x) \leq C_1 e^{-\|x\|^2/2}$ .
- (A2) For all  $t \in [0, \gamma]$ , the functions  $\rho_t$  and  $\hat{\rho}_t$  are continuously differentiable on  $\mathbb{R}^d$ , and their gradients satisfy  $\|\nabla \log \rho_t(x)\|, \|\nabla \log \hat{\rho}_t(x)\| \leq L(1 + \|x\|)$  for all  $x \in \mathbb{R}^d$ .
- (A3) For all  $t \in [0, \gamma]$ , the integral  $\int_{\mathbb{R}^d} (1 + \|x\|)^2 (\rho_t^3 / \hat{\rho}_t^2)(x) \, dx \leq C_2$ .

Moreover, under the additional Assumption 3, the Wasserstein gradient flow converges exponentially to  $q$  in terms of the  $\chi^2$ -divergence measure.

**Proposition 5** (Xu et al. (2024a), Prop. 4.1) Under Assumptions 1-3, the following holds:

$$\chi^2(p_n \| q) \leq e^{-2\gamma n} \chi^2(p_0 \| q) + \frac{C_4}{1 - e^{-2\gamma}} \epsilon^{1/2}, \quad (11)$$

for  $n = 1, 2, \dots$ , where the constant  $C_4$ , defined in equation (20), depends on  $C_1, C_2, L, \gamma$ .

Therefore, when all  $\beta_k$  are set to 1 and a static Wasserstein regularization is used in place of the dynamic Wasserstein regularization introduced in (9), our AF retains the well-established convergence properties for log-concave  $q$  as stated in Theorem 1 and Proposition 5, in terms of both the  $W_2$ -distance and the  $\chi^2$ -divergence measure. Furthermore, for non-log-concave densities  $q$ , we have established in Proposition 4 that the difference in the optimal velocity field between two consecutive annealing densities equals the score difference, under the unique dynamic optimal transport (OT) objective of our AF.

## C Experimental Details

### C.1 Evaluation metrics

To assess the performance of our model, we utilized two key metrics: Maximum Mean Discrepancy (MMD) and Wasserstein Distance, both of which measure the divergence between the true samples and the samples generated by the algorithms.

#### *Maximum Mean Discrepancy (MMD)*

MMD is a non-parametric metric used to quantify the difference between two distributions based on samples. Given two sets of samples  $X_1 \in \mathbb{R}^{n_1 \times d}$  and  $X_2 \in \mathbb{R}^{n_2 \times d}$ , MMD computes the kernel-based distances between these sets. Specifically, we employed a Gaussian kernel:

$$k(x, y) = \exp\{-\alpha\|x - y\|_2^2\},$$

parameterized by a bandwidth  $\alpha$ . The MMD is computed as follows:

$$\text{MMD}(X_1, X_2) = \frac{1}{n_1^2} \sum_{i,j} k(X_1^i, X_1^j) + \frac{1}{n_2^2} \sum_{i,j} k(X_2^i, X_2^j) - \frac{2}{n_1 n_2} \sum_{i,j} k(X_1^i, X_2^j),$$

where  $k(\cdot, \cdot)$  represents the Gaussian kernel. In our experiments, we set  $\alpha = 1/\gamma^2$  and  $\gamma = 0.1 \cdot \text{median\_dist}$ , where  $\text{median\_dist}$  denotes the median of the pairwise distances between the two datasets.

#### *Wasserstein Distance*

In addition to MMD, we used the Wasserstein distance, which measures the cost of transporting mass between distributions. Given two point sets  $X \in \mathbb{R}^d$  and  $Y \in \mathbb{R}^d$ , we compute the pairwise Euclidean distance between the points. The Wasserstein distance is then computed using the optimal transport plan via the linear sum assignment method (from `scipy.optimize` package):

$$W(X, Y) = \frac{1}{n} \sum_{i=1}^n \|X_{r(i)} - Y_{c(i)}\|_2,$$

where  $r(i)$  and  $c(i)$  are the optimal row and column assignments determined through linear sum assignment.

#### *Mode-Weight Mean Squared Error*

To compute the mode-weight mean squared error (MSE) in multi-modal experimental settings, we assign each sample to its closest mode, calculate the weights for each mode, and report the mean squared error between the sample weights and the true mode weights. The standard deviation is reported across 10 sampling iterations.

In all experiments, we sample 10,000 points from each model and generate 10,000 true samples from the GMM to calculate and report both MMD and Wasserstein distance. Note that the smaller the two metrics mentioned above, the better the sampling performance.

### C.2 Hutchinson trace estimator

The objective functions in (10) and (11) involve the calculation of  $\nabla \cdot \mathbf{v}_{\mathbf{k}}(x, t)$ , i.e., the divergence of the velocity field represented by a neural network. This may be computed by brute force using reverse-mode automatic differentiation, which is much slower and less stable in high dimensions.

We can express  $\nabla \cdot \mathbf{v}_{\mathbf{k}}(x, t) = \mathbb{E}_{\epsilon \sim N(0, I_d)} [\epsilon^T J_v(x) \epsilon]$ , where  $J_v(x)$  is the Jacobian of  $\mathbf{v}_{\mathbf{k}}(x, t)$  at  $x$ . Given a fixed  $\epsilon$ , we have  $J_v(x) \epsilon = \lim_{\sigma \rightarrow 0} \frac{\mathbf{v}_{\mathbf{k}}(x + \sigma \epsilon) - \mathbf{v}_{\mathbf{k}}(x)}{\sigma}$ , which is the directional derivative of  $\mathbf{v}_{\mathbf{k}}$  along the direction  $\epsilon$ . Thus, for a sufficiently small  $\sigma > 0$ , we can propose the following estimator (Hutchinson, 1989; Xu et al., 2024b):

$$\nabla \cdot \mathbf{v}_{\mathbf{k}}(x, t) \approx \mathbb{E}_{\epsilon \sim N(0, I_d)} \left[ \epsilon^T \frac{\mathbf{v}_{\mathbf{k}}(x + \sigma \epsilon, t) - \mathbf{v}_{\mathbf{k}}(x, t)}{\sigma} \right]. \quad (20)$$

This approximation becomes exact as  $\sigma \rightarrow 0$ . In our experiments, we set  $\sigma = 0.02/\sqrt{d}$ .

### C.3 Other Annealing Flow settings

#### *Time steps and numerical integration*

By selecting  $K$  values of  $\beta$ , we divide the original time scale  $[0, 1]$  of the Continuous Normalizing Flow (2) and (3) into  $K$  intervals:  $[t_{k-1}, t_k]$  for  $k = 1, 2, \dots, K$ . Notice that the learning of each velocity field  $\mathbf{v}_k$  depends only on the samples from the  $(k-1)$ -th block, not on the specific time stamp. Therefore, we can re-scale each block's time interval to  $[0, 1]$ , knowing that using the time stamps  $[(k-1)h, kh]$  yields the same results as using  $[0, 1]$  for the neural network  $\mathbf{v}_k(x, t)$ . For example, the neural network will learn  $\mathbf{v}_k(x, 0) = \mathbf{v}_k(x, (k-1)h)$  and  $\mathbf{v}_k(x, 1) = \mathbf{v}_k(x, kh)$ , regardless of the time stamps.

Recall that we relaxed the shortest transport map path into a dynamic  $W_2$  regularization loss via Proposition 2. This requires calculating intermediate points  $x(t_{k-1,s})$ , where  $s = 0, 1, \dots, S$ . We set  $S = 3$ , evenly spacing the points on  $[t_{k-1}, t_k]$ , resulting in the path points  $x(t_{k-1}), x(t_{k-1} + h_k/3), x(t_{k-1} + 2h_k/3), x(t_k)$ . To compute each  $x(t_{k-1,s})$ , we integrate the velocity field  $\mathbf{v}_k$  between  $t_{k-1}$  and  $t_{k-1,s}$ , using the Runge-Kutta method for numerical integration. Additionally, for each  $x(t_{k-1,s})$ , we calculate the velocity field at an intermediate time step between  $t_{k-1,s-1}$  and  $t_{k-1,s}$  to enable accurate numerical integration. Specifically, to calculate  $x(t+h)$  based on  $x(t)$  and an intermediate time stamp  $t + \frac{h}{2}$ :

$$\begin{aligned} x(t+h) &= x(t) + \frac{h}{6}(k_1 + 2k_2 + 2k_3 + k_4), \\ k_1 &= \mathbf{v}(x(t), t), \quad k_2 = \mathbf{v}\left(x(t) + \frac{h}{2}k_1, t + \frac{h}{2}\right), \\ k_3 &= \mathbf{v}\left(x(t) + \frac{h}{2}k_2, t + \frac{h}{2}\right), \quad k_4 = \mathbf{v}(x(t) + hk_3, t+h) \end{aligned}$$

Here,  $h$  is the step size, and  $\mathbf{v}(x, t)$  represents the velocity field.

#### *The choice of $\beta_k$*

In the experiments on Gaussian Mixture Models (GMMs), we set the number of intermediate  $\beta_k$  values to 8, equally spaced such that  $\beta_0 = 0, \beta_1 = 1/8, \beta_2 = 2/8, \dots, \beta_8 = 1$ . We chose the easy-to-sample distribution  $\pi_0(x)$  as  $N(0, I_d)$ . Finally, we added 2 refinement blocks. The intermediate distributions are defined as:

$$\tilde{f}_k(x) = \pi_0(x)^{1-\beta_k} \tilde{q}(x)^{\beta_k}.$$

In the experiment on the Truncated Normal Distribution, we did not select  $\beta_k$  in the same manner as for the GMM and Exp-Weighted Gaussian distributions. Instead, following the same Annealing philosophy, we construct a gradually transforming bridge from  $\pi_0(x)$  to  $\tilde{q}(x) = 1_{|x| \geq c} N(0, I_d)$  by setting each intermediate density as:

$$\tilde{f}_k(x) = 1_{\|x\| \geq c/(k+1)} N(0, I_d).$$

The number of intermediate  $\beta_k$  values is set to 8.

In the experiment on funnel distributions, we set all  $\beta_k = 1$ , with the number of time steps set to 8. As discussed in Appendix B, the algorithm becomes equivalent to a Wasserstein gradient descent problem.

In the experiment on 50D Exp-Weighted Gaussian, 20 time steps are used, with 15 intermediate densities and 5 refinement blocks.

#### *The choice of $\alpha$*

In the experiments on Gaussian Mixture Models (GMMs), funnel distributions, truncated normal, and Bayesian Logistic Regressions,  $\alpha$  is uniformly set to  $[\frac{8}{3}, \frac{8}{3}, \frac{4}{3}, \frac{4}{3}, \frac{2}{3}, \frac{2}{3}, \frac{2}{3}, \dots]$ . In the experiments on Exp-Weighted Gaussian,  $\alpha$  is set to  $[\frac{20}{3}, \frac{20}{3}, \frac{20}{3}, \frac{20}{3}, \frac{10}{3}, \frac{10}{3}, \frac{10}{3}, \frac{10}{3}, \frac{5}{3}, \frac{5}{3}, \frac{5}{3}, \frac{5}{3}, 1, 1, 1, 1, 1, 1, 1, 1, 1, 1]$ .

#### *The objective*

Note that the objective (10) for  $v_k(x(t), t)$ ,  $t \in (t_{k-1}, t_k]$  is independent of  $\tilde{E}_k(x(t_{k-1}))$ . During the experiments, we found that using the Taylor approximation of around  $x(t_k)$ :  $\tilde{E}_k(x(t_{k-1})) - \tilde{E}_k(x(t_k)) \approx (-h_k) \nabla E(x(t_k)) \cdot \mathbf{v}_k$ , and replacing the energy function  $\tilde{E}_k(x(t_k))$  generally led to slightly better performance. In our experiments on the GMM, Funnel distribution, and Exp-weighted Gaussian, we consistently used this form. For the experiments on the Truncated Normal and Bayesian Logistic Regression, the original  $\tilde{E}_k(x(t_k))$  was used.

#### *Neural networks and selection of other hyperparameters*

The neural network structure in our experiments is consistently set with hidden layers of size 32-32. During implementation, we observed that when  $d \leq 5$ , even a neural network with a single hidden layer of size 32 can perform well for sampling. However, for consistency across all experiments, we uniformly set the structure to 32-32.

We sample 100,000 data points from  $N(0, I_d)$  for training, with a batch size of 1,000. The Adam optimizer is used with a learning rate of 0.0001, and the maximum number of iterations for each block  $\mathbf{v}_k$  is set to 1,000. An additional two blocks are added for refinement after  $\beta_K = 1$ .

Different numbers of test samples are used for reporting the experimental results: 5,000 points are sampled and plotted for the experiment on Gaussian Mixture Models, 5,000 points for the experiment on Truncated Normal Distributions, 10,000 points for the experiment on Funnel Distributions, and 10,000 points for the experiment on Exp-Weighted Gaussian with 1,024 modes in 10D space.

## C.4 Bayesian logistic regression

We use a hierarchical Bayesian structure for logistic regression across a range of datasets provided by LIBSVM. The detailed setting of the Bayesian Logistic Regression is as follows.

We adopt the same Bayesian logistic regression setting as described in Liu & Wang (2016), where a hierarchical structure is assigned to the model parameters. The weights  $\beta$  follow a Gaussian prior,  $p_0(\beta|\alpha) = N(\beta; 0, \alpha^{-1})$ , and  $\alpha$  follows a Gamma prior,  $p_0(\alpha) = \text{Gamma}(\alpha; 1, 0.01)$ . The datasets used are binary, where  $x_i$  has a varying number of features, and  $y_i \in \{+1, -1\}$  across different datasets. Sampling is performed from the posterior distribution:

$$p(\beta, \alpha|D) \propto \text{Gamma}(\alpha; 1, 0.01) \cdot \prod_{d=1}^D N(\beta_d; 0, \alpha^{-1}) \cdot \prod_{i=1}^n \frac{1}{1 + \exp(-y_i \beta^T x_i)},$$

We set  $\beta_k = 1$  and use 8 blocks to train the Annealing Flow.

During testing, we use all algorithms to sample 1,000 particles of  $\beta$  and  $\alpha$  jointly, and use  $\{\beta^{(i)}\}_{i=1}^{1000}$  to construct 1,000 classifiers. The mean accuracy and standard deviation are then reported in Table 4. Additionally, the average log posterior in Table 4 is reported as:

$$\frac{1}{|D_{\text{test}}|} \sum_{x, y \in D_{\text{test}}} \log \frac{1}{|C|} \sum_{\theta \in C} p(y|x, \theta).$$

## C.5 Importance flow

We report the results of the importance sampler (discussed in Section 5) for estimating  $\mathbb{E}_{x \sim N(0, I)} [1_{\|x\| \geq c}]$  with varying  $c$  and dimensions, based on our Annealing Flow. To estimate  $\mathbb{E}_{x \sim N(0, I)} [1_{\|x\| \geq c}]$ , we know that the theoretically optimal proposal distribution which can achieve 0 variance is  $\tilde{q}^*(x) = 1_{\|x\| \geq c} N(0, I)$ . Then the estimator becomes:

$$\mathbb{E}_{X \sim \pi_0(x)} [h(X)] = \mathbb{E}_{X \sim q^*(x)} \left[ \frac{\pi_0(x)}{q^*(x)} \cdot h(x) \right] \approx \frac{1}{n} \sum_{i=1}^n \frac{\pi_0(x_i)}{q^*(x_i)} \cdot h(x_i), \quad x_i \sim q^*(x),$$

where  $\pi_0(x) = N(0, I_d)$ ,  $h(x) = 1_{\|x\| \geq c}$  and  $q^*(x) = Z \cdot \tilde{q}^*(x)$ .

Therefore, the Importance Flow consists of two parts: First, using Annealing Flow to sample from  $\tilde{q}^*(x)$ ; second, constructing a Density Ratio Estimation (DRE) neural network using samples from  $\{x_i\}_{i=1}^n \sim \tilde{q}^*(x)$  and  $\{y_i\}_{i=1}^n \sim N(0, I_d)$ , as discussed in Section 5.2. The estimator becomes:

$$\frac{1}{n} \sum_{i=1}^n \text{DRE}(x_i) \cdot h(x_i).$$

The Naive MC results comes from directly using  $\{y_i\}_{i=1}^n \sim N(0, I_d)$  to construct estimator  $\frac{1}{n} \sum_{i=1}^n 1_{\|y_i\| \geq c}$ . When  $c \geq 6$ , the Naive MC methods consistently output 0 as the result.

In our experiment, we use a single DRE neural network to construct the density ratio between  $\pi_0(x)$  and  $q^*(x) = Z \cdot 1_{\|x\| \geq c} N(0, I)$  directly. The neural network structure consists of hidden layers with sizes 64-64-64. The size of the training data is set to 100,000, and the batch size is set to 10,000. We use 30 to 70 epochs for different distributions, depending on the values of  $c$  and dimension  $d$ . The Adam optimizer is used, with a learning rate of 0.0001. The test data size is set to 1,000, and all results are based on 200 estimation rounds, each using 500 samples.

---

**Algorithm 2** Metropolis-Hastings Algorithm

---

```
1: Initialize  $x_0$ 
2: for  $t = 1$  to  $N$  do
3:   Propose  $x^* \sim q(x^*|x_{t-1})$ 
4:   Compute acceptance ratio  $\alpha = \min\left(1, \frac{\pi(x^*)q(x_{t-1}|x^*)}{\pi(x_{t-1})q(x^*|x_{t-1})}\right)$ 
5:   Sample  $u \sim \text{Uniform}(0, 1)$ 
6:   if  $u < \alpha$  then
7:      $x_t = x^*$ 
8:   else
9:      $x_t = x_{t-1}$ 
10:  end if
11: end for
12: return  $\{x_t\}_{t=0}^N$ 
```

---

---

**Algorithm 3** Hamiltonian Monte Carlo (HMC)

---

```
1: Initialize  $x_0$ 
2: for  $t = 1$  to  $N$  do
3:   Sample  $p \sim \mathcal{N}(0, M)$ 
4:   Set  $(x, p) \leftarrow (x_{t-1}, p)$ 
5:   for  $i = 1$  to  $L$  do
6:      $p \leftarrow p - \frac{\epsilon}{2} \nabla U(x)$ 
7:      $x \leftarrow x + \epsilon M^{-1} p$ 
8:      $p \leftarrow p - \frac{\epsilon}{2} \nabla U(x)$ 
9:   end for
10:  Compute acceptance ratio  $\alpha = \min(1, \exp(H(x_{t-1}, p_{t-1}) - H(x, p)))$ 
11:  Sample  $u \sim \text{Uniform}(0, 1)$ 
12:  if  $u < \alpha$  then
13:     $x_t = x$ 
14:  else
15:     $x_t = x_{t-1}$ 
16:  end if
17: end for
18: return  $\{x_t\}_{t=0}^N$ 
```

---

---

**Algorithm 4** Parallel Tempering Algorithm

---

```
1: Initialize replicas  $\{x_1, x_2, \dots, x_{\text{num\_replicas}}\}$  with Gaussian noise
2: Initialize temperatures  $\{T_1, T_2, \dots, T_{\text{num\_replicas}}\}$ 
3: for  $i = 1$  to iterations do
4:   for  $j = 1$  to num_replicas do
5:     Propose  $x_j^* \sim q(x_j^*|x_j)$  {Using Metropolis-Hastings step for each replica}
6:     Compute acceptance ratio  $\alpha_j = \frac{\pi(x_j^*)}{\pi(x_j)}$ 
7:     Sample  $u \sim \text{Uniform}(0, 1)$ 
8:     if  $u < \alpha_j$  then
9:        $x_j = x_j^*$ 
10:    end if
11:    Store  $x_j$  in samples for replica  $j$ 
12:  end for
13:  if  $i \bmod \text{exchange\_interval} = 0$  then
14:    for  $j = 1$  to num_replicas - 1 do
15:      Compute energies  $E_j = -\log(\pi(x_j) + \epsilon)$ ,  $E_{j+1} = -\log(\pi(x_{j+1}) + \epsilon)$ 
16:      Compute  $\Delta = \left(\frac{1}{T_j} - \frac{1}{T_{j+1}}\right)(E_{j+1} - E_j)$ 
17:      Sample  $u \sim \text{Uniform}(0, 1)$ 
18:      if  $u < \exp(\Delta)$  then
19:        Swap  $x_j \leftrightarrow x_{j+1}$ 
20:      end if
21:    end for
22:  end if
23: end for
24: return samples from all replicas
```

---



## C.6 Details of other algorithms

The Algorithm 2, 3, and 4 introduce the algorithmic framework of Metropolis-Hastings (MH), Hamiltonian Monte Carlo (HMC), and Parallel Tempering (PT) compared in our experiments.

In our experiments, we set the proposal density as  $q(x'|x) = \mathcal{N}(x; 0, I_d)$ . We use 5 replicas in Parallel Tempering (PT), with a linear temperature progression ranging from  $T_1 = 1.0$  to  $T_{\max} = 2.0$ , and an exchange interval of 100 iterations. For HMC, we set the number of leapfrog steps to 10, with a step size ( $\epsilon$ ) of 0.01, and the mass matrix  $M$  is set as the identity matrix. Additionally, we use the default hyperparameters as specified in SVGD (Liu & Wang, 2016), MIED (Li et al., 2023), and AI-Sampler (Egorov et al., 2024). In the actual implementation, we found that the time required for SVGD to converge increases significantly with the number of samples. Therefore, in most experiments, we sample 1000 data points at a time using SVGD, aggregate the samples, and then generate the final plot.

## D Additional Experiment Details and Results

We adopt the standard Annealing Flow framework discussed in this paper for experiments on Gaussian Mixture Models (GMM), Truncated Normal distributions, and Exp-Weighted Gaussian distributions. For experiments on funnel distributions, we set each  $\tilde{f}_k(x)$  as the target  $q(x)$ , under which the Annealing Flow objective becomes equivalent to the Wasserstein Gradient Flow based on the JKO scheme, as discussed in B. Please refer to C.3 for  $\beta_k$  selections.

### D.1 More Results

#### Gaussian Mixture Models (GMMs)

We tested each algorithm on GMMs with dimensions ranging from 2 to 5. In the 2D GMM, the modes are arranged in circles with radii  $r = 8, 10, 12$ . For dimensions higher than 2, the coordinates of the additional dimensions are set to  $r/2$ .

Figure 5 shows the results when the number of time steps for CRAFT, LFIS, and PGPS is set to 10, the same as for AF. Additionally, Figure 5 presents results where the number of time steps for CRAFT, LFIS, and PGPS is set to 128, 256, and 128, respectively, while the time step for AF remains at 10.

In Tables 2 and 3, the results for CRAFT, LFIS, and PGPS are shown with the number of time steps set to 10, matching that of AF for fair comparison.

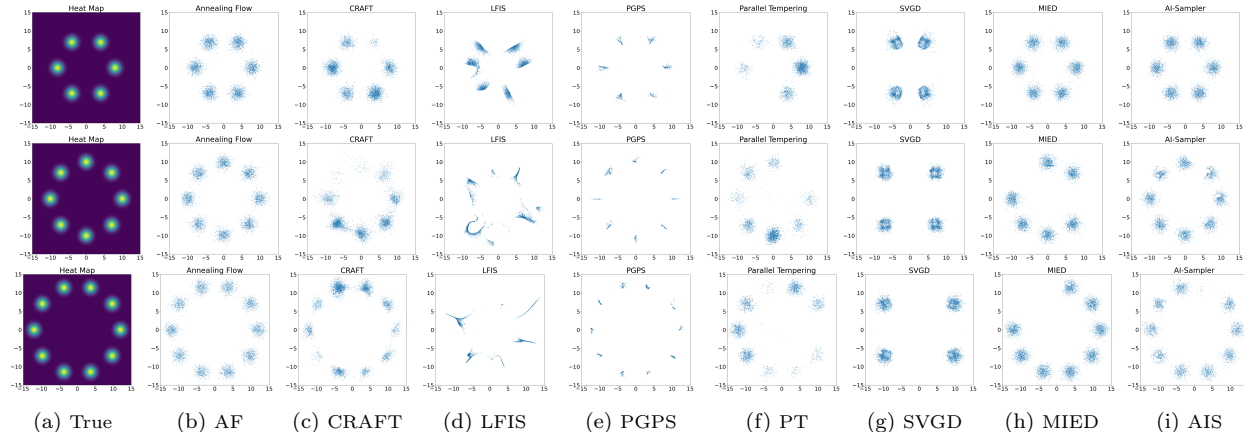


Figure 4: Sampling methods for Gaussian Mixture Models (GMM) with 6, 8, and 10 modes arranged on circles with radii  $r = 8, 10, 12$ . The number of time steps for CRAFT, LFIS, and PGPS is set to 10, the same as for AF.

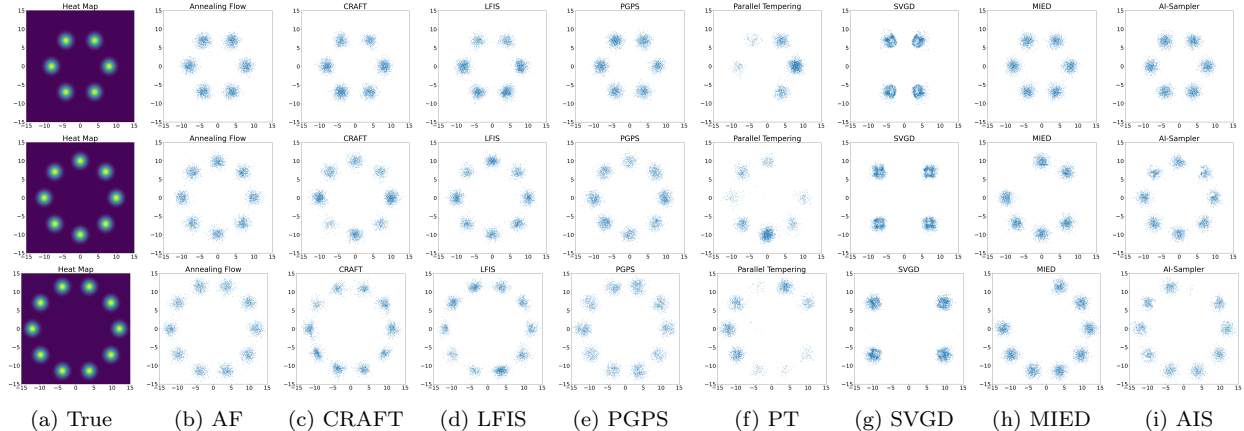


Figure 5: Sampling methods for Gaussian Mixture Models (GMM) with 6, 8, and 10 modes arranged on circles with radii  $r = 8, 10, 12$ . The number of time steps for AF is 10. The number of time steps for CRAFT, LFIS, and PGPS is set as 128, 256, and 128, respectively.

### Truncated Normal Distribution

Relaxations are applied to the Truncated Normal Distribution in all experiments except for MH, HMC, and PT. Specifically, we relax the indicator function  $1_{\|x\| \geq c}$  to  $\frac{1}{1 + \exp(-k(\|x\| - c))}$ . We set  $k = 20$  for all experiments. AIS is designed for continuous densities, and we similarly relax the densities in SVGD and MIED, following the approach used in AF. The resulting plots are as follows:

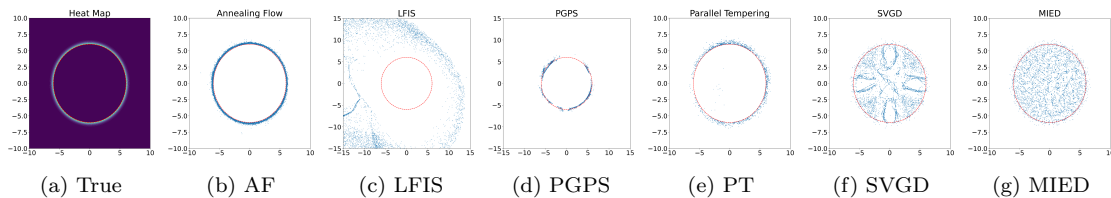


Figure 6: Sampling Methods for Truncated Normal Distributions with Radius  $c = 6$ , together with the failure cases of SVGD and MIED.

Each algorithm draws 5,000 samples. It can be observed that MCMC-based methods, including HMC and PT, produce many overlapping samples. This occurs because when a new proposal is rejected, the algorithms retain the previous sample, leading to highly correlated sample sets.

Table 5: Proportion of Annealing Flow Samples Within  $c$ , Across Different Dimensions

Proportion Within $c$	$c = 4$	$c = 6$	$c = 8$
$D = 2$	0.17%	0.18%	1.78%
$D = 3$	0.20%	0.23%	3.23%
$D = 4$	0.68%	1.48%	3.68%
$D = 5$	1.46%	3.37%	4.12%
$D = 10$	2.13%	4.68%	7.13%

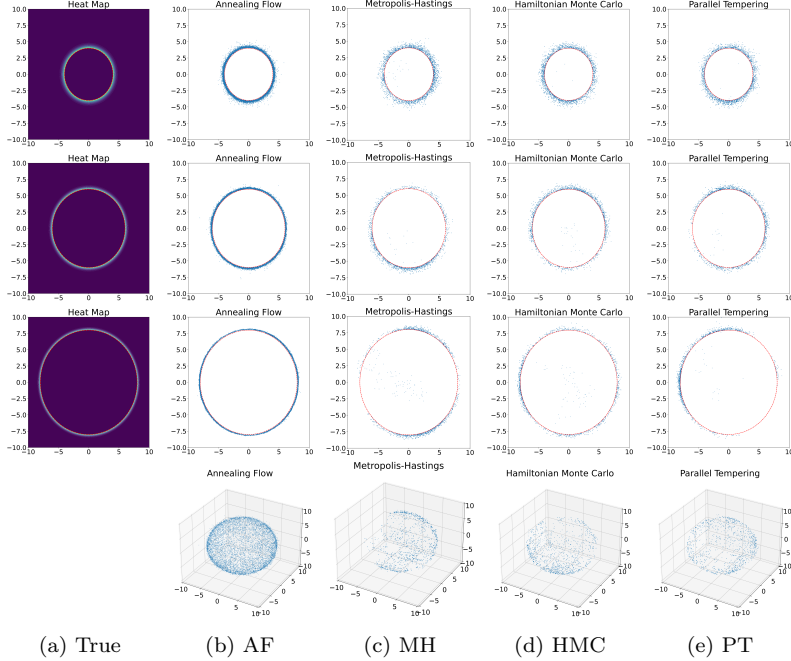


Figure 7: Sampling methods for truncated normal distributions with radii  $c = 6$  and  $c = 8$  in 2D space for the first two rows. The last row presents sampling results in  $5D$  with a radius of 8, projected onto a  $3D$  space.

For dimensions  $d > 2$ , visualizing the results by comparing the sample positions using a red sphere surface becomes challenging. Therefore, we calculate the proportion of samples within radius  $c$ . A lower proportion indicates better sampling performance. Table 5 presents these results. We also calculate the proportion of the surface  $\|x\| = c$  covered by the samples for AF, MH, HMC, and PT. In all experiments with the Truncated Normal distribution, AF covers more than 95% of the surface area. However, when  $d \geq 3$  and  $c \geq 6$ , all other methods cover less than 70% of the surface area.

### Funnel Distribution

In the main paper, we present the sampling methods for the funnel distribution with  $d = 5$ , projected onto a  $3D$  space. To assess the sample quality, here we present the corresponding results projected onto a  $2D$  space, plotted alongside the density heat map.

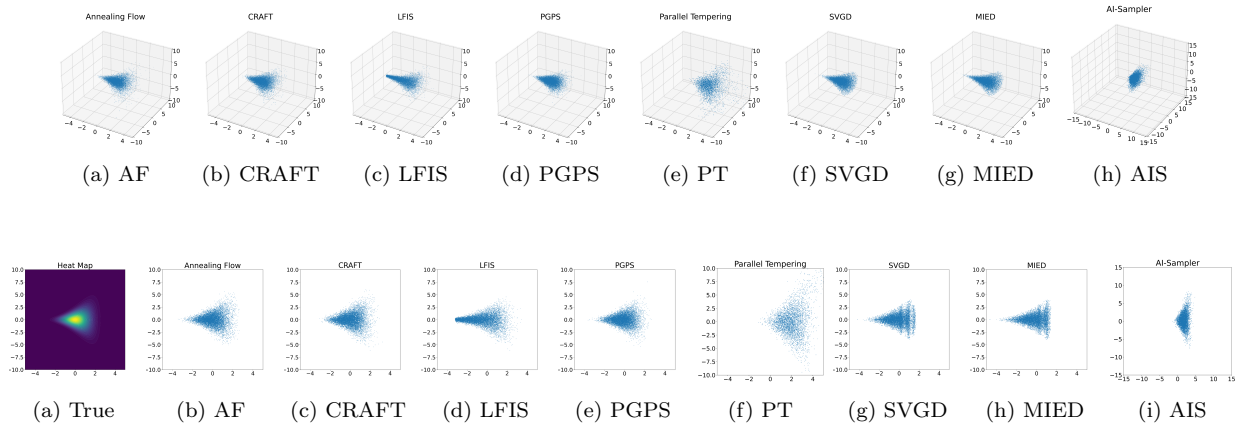


Figure 9: Sampling Methods for Funnel Distribution with  $\sigma^2 = 0.81$  in Dimension  $d = 5$ , projected onto a  $d = 3$  Space.

As seen from both figures, our AF method achieves the best sampling performance on the funnel distribution, while other methods, such as MIED and AIS, fail to capture the full spread of the funnel’s tail. Additionally, PT, SVGD, and AIS all fail to capture the sharp part of the funnel’s shape.

*Exp-Weighted Gaussian Distribution*

Table 1 in the main manuscript presents results for CRAFT, LFIS, and PGPS, using the same number of intermediate time steps as AF. Below, in Table 6, we report the number of modes explored for the 50D Exp-Weighted Gaussian distribution when CRAFT, LFIS, and PGPS are trained with 128, 256, and 128 time steps, respectively.

Table 6: Number of Modes Explored in the Exp-Weighted Gaussian Distribution by Different Methods, with CRAFT, LFIS, and PGPS Trained with 128, 256, and 128 Time Steps, Respectively. AF is trained with 20 Time Steps.

	True	AF	CRAFT	LFIS	PGPS	PT	SVGD	MIED	AIS
$d = 2$	4	<b>4</b>	<b>4</b>	<b>4</b>	<b>4</b>	3.4	3.9	3.8	3.8
$d = 5$	32	<b>32</b>	30.3	31.6	<b>32</b>	25.2	28.5	28.0	28.3
$d = 10$	1024	<b>1024</b>	984.0	993.2	1002.8	233.7	957.3	923.4	301.2
$d = 50$	1024	<b>1024</b>	886.5	923.4	994.0	< 10	916.4	890.6	125.6

*Importance Flow*

Table 7 reports the preliminary results of the importance flow (discussed in Section 5) for estimating  $\mathbb{E}_{x \sim N(0, I)} [1_{\|x\| \geq c}]$  with varying radii  $c$  and dimensions. This estimation uses samples from the experiment on the Truncated Normal Distribution, and thus the results for SVGD, MIED, and AIS cannot be reported. Additionally, we discussed a possible extension of the Importance Flow framework in D.4.

Table 7: Comparison of estimation results for  $\mathbb{E}_{x \sim N(0, I)} [1_{\|x\| > c}]$  across different radii  $c$  and dimensions  $d$ . Values in parentheses represent the standard deviation.

Methods	Radius	$d = 2$	$d = 3$	$d = 4$	$d = 5$
True Probability	$c = 4$	3.35e-04	1.13e-03	3.02e-03	6.84e-03
	$r = 6$	1.52e-08	7.49e-08	2.89e-07	9.50e-07
Importance Flow	$c = 4$	<b>4.04e-04(1.0e-04)</b>	1.30e-03(2.3e-04)	<b>3.36e-03(4.23e-04)</b>	<b>7.86e-03(8.21e-04)</b>
	$c = 6$	<b>9.81e-08(4.02e-07)</b>	<b>1.51e-07(1.23e-07)</b>	<b>2.13e-07(8.71e-08)</b>	<b>2.38e-07(3.48e-06)</b>
DRE with HMC Samples	$c = 4$	7.56e-04(4.99e-04)	2.52e-03(6.33e-04)	8.97e-03(9.05e-04)	1.12e-02(1.55e-03)
	$c = 6$	4.35e-07(7.21e-07)	9.01e-07(2.79e-06)	1.82e-07(2.89e-06)	2.31e-06(6.21e-06)
DRE with PT Samples	$c = 4$	6.79e-04(3.58e-04)	2.38e-03(5.40e-04)	5.78e-03(7.98e-03)	9.94e-03(1.13e-03)
	$c = 6$	5.37e-07(9.56e-07)	8.78e-07(2.32e-06)	9.23e-07(2.51e-06)	1.98e-06(7.73e-06)
Naïve MC	$c = 4$	2.75e-04(6.0e-04)	<b>1.18e-03(1.1e-03)</b>	<b>2.71e-03(1.7e-03)</b>	7.94e-03(2.6e-03)
	$c = 6$	0	0	0	0

**D.2 Training Efficiency**

Table 8 presents the training and sampling times for AF, CRAFT, LFIS, and PGPS in experiments on a 50D Exp-Weighted Gaussian distribution, conducted on an A100 GPU. The training setup includes 100,000 samples, 1,000 training iterations per time step, and a batch size of 1,000 for AF, CRAFT, and PGPS. For LFIS, a batch size of 5,000 is used to ensure good performance. The sampling time is measured for generating 10,000 samples. AF achieves optimal sampling performance with only 20 time steps, compared to other methods requiring up to 256 time steps. Specifically, CRAFT and PGPS were trained with 128 time steps, while LFIS used 256 time steps, ensuring these methods achieved the results shown in Figure 5 and Table 6.

Table 8: Total Training and Sampling Time Comparison for the 50D Exp-Weighted Gaussian

Methods	Training time (mins)	Sampling time (s)
AF	<b>14.5 ± 1.3</b>	<b>2.1 ± 0.5</b>
CRAFT	51.2 ± 1.8	4.9 ± 0.6
LFIS	86.4 ± 3.5	6.4 ± 0.6
PGPS	59.7 ± 2.1	5.2 ± 0.4

Table 9 reports the training and sampling times per time step (block) for each method. Notably, as AF requires

numerical integration over the velocity field, its training time per time step is slightly higher compared to other methods.

Table 9: Training and Sampling Time Comparison Per Time Step for the 50D Exp-Weighted Gaussian

Methods	Training time (mins)	Sampling time (s)
AF	$0.70 \pm 0.10$	$0.10 \pm 0.02$
CRAFT	$0.45 \pm 0.09$	$0.06 \pm 0.01$
LFIS	$0.37 \pm 0.07$	$0.04 \pm 0.01$
PGPS	$0.44 \pm 0.10$	$0.04 \pm 0.01$

### D.3 Ablation Studies

As reported in the main manuscript, we use 8 intermediate densities and 2 refinement blocks for the GMM experiments, and 15 intermediate densities with 5 refinement blocks for the 50D Exp-Weighted Gaussian experiments. For GMMs, the regularization constant  $\alpha$  is set to  $[\frac{8}{3}, \frac{8}{3}, \frac{4}{3}, \frac{4}{3}, \frac{2}{3}, \frac{2}{3}, \frac{2}{3}, \dots]$ . For Exp-Weighted Gaussian,  $\alpha$  is set to  $[\frac{20}{3}, \frac{20}{3}, \frac{20}{3}, \frac{20}{3}, \frac{10}{3}, \frac{10}{3}, \frac{10}{3}, \frac{10}{3}, \frac{5}{3}, \frac{5}{3}, \frac{5}{3}, \frac{5}{3}, 1, 1, 1, 1, 1, 1, 1]$ .

In our main experiments, we note that CRAFT, LFIS, and PGPS require 128, 256, and 128 time steps, respectively, to achieve comparable performance. In this section, we conduct additional ablation studies to investigate the role of annealing densities and Wasserstein regularization in ensuring the smoothness and success of Annealing Flow, particularly when fewer time steps are used. We also compare the performance of all NF methods under further reduced time steps.

#### D.3.1 Significance of annealing densities and Wasserstein regularization

Here, we conduct experiments on GMMs *without* intermediate densities (i.e., all  $f_k(x) = q(x)$ ) and using 5 blocks. In Figure 10, the second column shows AF with the regularization constant  $\alpha$  set to  $[\frac{4}{3}, \frac{4}{3}, \frac{2}{3}, \frac{2}{3}, \frac{2}{3}]$ , the third column with  $\alpha$  set to  $[\frac{8}{3}, \frac{8}{3}, \frac{4}{3}, \frac{4}{3}, \frac{4}{3}]$ , and the fourth column with  $\alpha$  set to  $[\frac{20}{3}, \frac{20}{3}, \frac{8}{3}, \frac{8}{3}, \frac{8}{3}]$ .

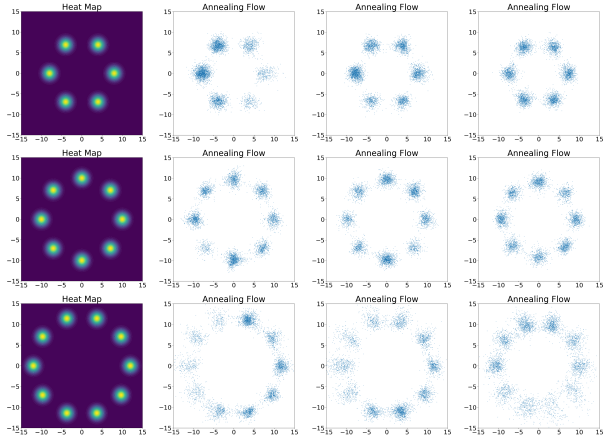


Figure 10: Ablation Studies for Gaussian Mixture Models (GMM) with 6, 8, and 10 modes arranged on circles with radii  $r = 8, 10, 12$ . AF is trained with no intermediate densities and 5 training blocks. The regularization constant  $\alpha$  used in the experiments for the three columns is described in the first paragraph of D.3.1.

The figure illustrates an extreme training scenario with no intermediate annealing densities, where the target modes are far separated from the initial density  $\pi_0 = N(0, I)$ . By comparing this to the successful case, where AF is trained with 8 intermediate densities and 2 refinement blocks (Figure 5), one can immediately see that annealing procedures are essential for successfully handling far-separated modes.

Furthermore, in Figure 10, when no intermediate densities are used, increasing the Wasserstein regularization constant—particularly in the initial blocks—leads to improved results. This experimentally highlights the importance of Wasserstein regularization in our AF objective for ensuring stable performance and significantly reducing the number of intermediate time steps.

Table 10: Number of Modes Explored in the 50D Exponentially-Weighted Gaussian by Various Methods with Different Numbers of Annealing Densities  $K$ .

	AF	CRAFT	LFIS	PGPS
$K = 0$	18.4	4.8	3.2	6.0
$K = 2$	86.7	18.0	14.2	22.8
$K = 4$	284.3	128.6	108.0	148.0
$K = 6$	808.0	256.8	186.4	424.5
$K = 8$	996.2	382.0	208.4	578.8
$K = 10$	1024	406.2	234.0	689.0

For the challenging 50D Exponentially Weighted Gaussian with 1024 widely separated modes, where the two farthest modes are 63.25  $L_2$  distance apart, annealing procedures are mandatory to ensure success. Table 10 shows the number of modes explored in the 50D Exp-Weighted Gaussian by AF, CRAFT, LFIS, and PGPS as the number of annealing steps  $K$  increases. Together with Table 1, it is evident that our AF consistently requires the fewest annealing steps to achieve success in highly challenging scenarios, owing to the  $W_2$  regularization of our unique dynamic OT loss.

### D.3.2 Performance of algorithms with fewer annealing steps

In Figures 3 and 4, the number of time steps for AF, CRAFT, LFIS, and PGPS is set to 10. Here, in Figure 11, we present ablation studies comparing the performance of these four methods when the number of time steps is reduced to 5.

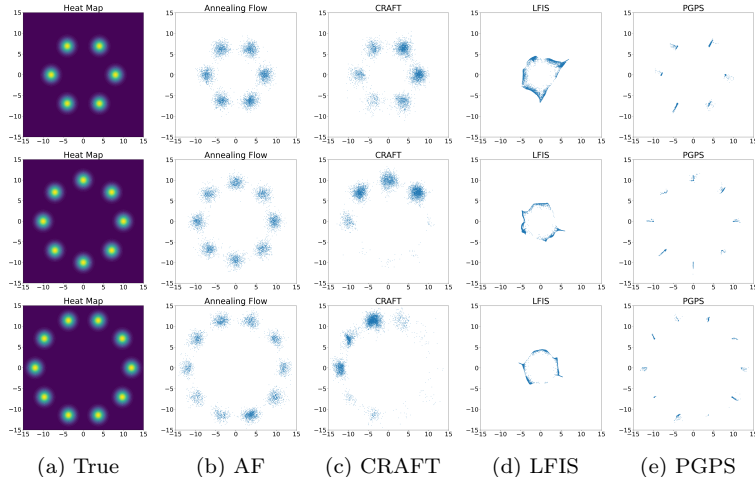


Figure 11: Ablation Studies for Gaussian Mixture Models (GMM) with 6, 8, and 10 modes arranged on circles with radii  $r = 8, 10, 12$ . All methods are trained with 4 intermediate densities and 1 refinement block.

It can be observed that even with half the number of time steps, AF maintains competitive performance on GMMs with 6 and 8 modes and significantly outperforms other methods on GMMs with 10 modes.

Table 11: Mode-Weight Mean Squared Error Across Distributions. The number of time steps for AF, CRAFT, LFIS, and PGPS is reduced to 15 from 20.

Distributions \ Methods	AF	CRAFT	LFIS	PGPS
$d = 10$ ExpGauss-1024	$7.2 \times 10^{-8} \pm 5.0 \times 10^{-9}$	$4.8 \times 10^{-6} \pm 3.3 \times 10^{-7}$	$7.3 \times 10^{-6} \pm 7.4 \times 10^{-7}$	$7.8 \times 10^{-7} \pm 7.0 \times 10^{-8}$
$d = 50$ ExpGauss-1024	$1.2 \times 10^{-7} \pm 9.5 \times 10^{-9}$	$7.2 \times 10^{-6} \pm 9.0 \times 10^{-7}$	$9.3 \times 10^{-6} \pm 8.2 \times 10^{-7}$	$9.8 \times 10^{-7} \pm 7.6 \times 10^{-8}$
$d = 50$ ExpGaussUV-2-1024	$1.1 \times 10^{-7} \pm 8.2 \times 10^{-9}$	$8.5 \times 10^{-6} \pm 8.9 \times 10^{-7}$	$9.9 \times 10^{-6} \pm 1.0 \times 10^{-6}$	$1.3 \times 10^{-6} \pm 9.0 \times 10^{-8}$
$d = 50$ ExpGaussUV-10-1024	$1.4 \times 10^{-7} \pm 9.6 \times 10^{-9}$	$9.2 \times 10^{-6} \pm 9.1 \times 10^{-7}$	$1.1 \times 10^{-5} \pm 1.3 \times 10^{-6}$	$1.9 \times 10^{-6} \pm 1.7 \times 10^{-7}$

We conducted similar ablation studies on the 50D Exp-Weighted Gaussian with 1024 widely separated modes, reducing the number of time steps from 20 to 15. Table 11 presents the mode-weight MSE in Exp-weighted Gaussian across different dimensions and unequal variances, when the number of time steps is reduced to 15 from 20 for all NF methods. AF still successfully captures all 1024 modes, with slightly higher Mode-Weight MSEs compared to the

values reported in Table 3. In contrast, other methods, including CRAFT, LFIS, and PGPS, perform much worse than AF.

## D.4 Possible Extensions of Importance Flow

The importance flow discussed and experimented with in this paper requires a given form of  $\pi_0(x)$ , and thus, a given form of  $\tilde{q}^*(x) = \pi_0(x) \cdot |h(x)|$  for estimating  $\mathbb{E}_{X \sim \pi_0(x)} [h(X)]$ . In our experimental settings,  $\tilde{q}^*(x) = 1_{\|x\| \geq c} \mathcal{N}(0, I_d)$  can be regarded as the Least-Favorable-Distribution (LFD). We conducted a parametric experiment for the case where  $\tilde{q}^*(x)$  has the given analytical form.

However, we believe future research may extend this approach to a distribution-free model. That is, given a dataset without prior knowledge of its distribution, one could attempt to learn an importance flow for sampling from its Least-Favorable Distribution (LFD) while minimizing the variance. For example, in the case of sampling from the LFD and obtaining a low-variance IS estimator for  $P_{x \sim \pi(x)}(\|x\| \geq c)$ , one may use the following distribution-free loss for learning the flow:

$$\min_{\theta} \frac{1}{n} \sum_{i=1}^n [1\{\mathcal{T}(x_i; \theta) \leq c\} \cdot \|\mathcal{T}(x_i; \theta) - c\|^2] + \gamma \int_0^1 \|\mathbf{v}(x(t), t; \theta)\|^2, \quad (21)$$

where the first term of the loss pushes the dataset  $\{x_i\}_{i=1}^n$  towards the Least-Favorable tail region, while the second term ensures a smooth and cost-optimal transport map. Note that the above loss assumes no prior knowledge of the dataset distribution  $\pi(x)$  or the target density  $q(x)$ .

Xu et al. (2024c) has also explored this to some extent by designing a distributionally robust optimization problem to learn a flow model that pushes samples toward the LFD  $Q^*$ , which is unknown and learned by the model through a risk function  $\mathcal{R}(Q^*, \phi)$ . Such framework has significant applications in adversarial attacks, robust hypothesis testing, and differential privacy. Additionally, the recent paper by Ribera Borrell et al. (2024) introduces a dynamic control loss for training a neural network to approximate the importance sampling control. We believe that by designing an optimal control loss in line with the approaches of these two papers, one can develop a distribution-free Importance Flow for sampling from the LFD of a dataset while minimizing the variance of the adversarial loss, which can generate a greater impact on the fields of adversarial attacks and differential privacy.

## References

- Michael S. Albergo and Eric Vanden-Eijnden. Learning to sample better, 2023. URL <https://arxiv.org/abs/2310.11232>. Les Houches 2022 Summer School on Statistical Physics and Machine Learning.
- Michael Arbel, Alex Matthews, and Arnaud Doucet. Annealed flow transport monte carlo. In *International Conference on Machine Learning*, pp. 318–330. PMLR, 2021.
- Sheldon Axler. *Measure, integration & real analysis*. Springer Nature, 2020.
- Maximilian Balandat, Brian Karrer, Daniel Jiang, Samuel Daulton, Ben Letham, Andrew G Wilson, and Eytan Bakshy. Botorch: A framework for efficient monte-carlo bayesian optimization. *Advances in neural information processing systems*, 33:21524–21538, 2020.
- Jean-David Benamou and Yann Brenier. A computational fluid mechanics solution to the monge-kantorovich mass transfer problem. *Numerische Mathematik*, 84(3):375–393, 2000.
- Luigi Bonati, Yue-Yu Zhang, and Michele Parrinello. Neural networks-based variationally enhanced sampling. *Proceedings of the National Academy of Sciences*, 116(36):17641–17647, 2019.
- Nawaf Bou-Rabee and Jesús María Sanz-Serna. Randomized hamiltonian monte carlo. 2017.
- James Brofos, Marylou Gabrié, Marcus A Brubaker, and Roy R Lederman. Adaptation of the independent metropolis-hastings sampler with normalizing flow proposals. In *International Conference on Artificial Intelligence and Statistics*, pp. 5949–5986. PMLR, 2022.
- Alberto Cabezas, Louis Sharrock, and Christopher Nemeth. Markovian flow matching: Accelerating mcmc with continuous normalizing flows. *arXiv preprint arXiv:2405.14392*, 2024.

- Joseph Carlson, Stefano Gandolfi, Francesco Pederiva, Steven C Pieper, Rocco Schiavilla, Kevin E Schmidt, and Robert B Wiringa. Quantum monte carlo methods for nuclear physics. *Reviews of modern physics*, 87(3):1067–1118, 2015.
- Rohitash Chandra, Konark Jain, Ratneel V Deo, and Sally Cripps. Langevin-gradient parallel tempering for bayesian neural learning. *Neurocomputing*, 359:315–326, 2019.
- Omar Chehab, Aapo Hyvarinen, and Andrej Risteski. Provable benefits of annealing for estimating normalizing constants: Importance sampling, noise-contrastive estimation, and beyond. *Advances in Neural Information Processing Systems*, 36, 2024.
- Xiuyuan Cheng, Jianfeng Lu, Yixin Tan, and Yao Xie. Convergence of flow-based generative models via proximal gradient descent in wasserstein space. *arXiv preprint arXiv:2310.17582*, 2023.
- Kristy Choi, Chenlin Meng, Yang Song, and Stefano Ermon. Density ratio estimation via infinitesimal classification. In *International Conference on Artificial Intelligence and Statistics*, pp. 2552–2573. PMLR, 2022.
- Michael CH Choi. Metropolis–hastings reversiblizations of non-reversible markov chains. *Stochastic Processes and their Applications*, 130(2):1041–1073, 2020.
- Adam D Cobb and Brian Jalaian. Scaling hamiltonian monte carlo inference for bayesian neural networks with symmetric splitting. In *Uncertainty in Artificial Intelligence*, pp. 675–685. PMLR, 2021.
- Rob Cornish, Paul Vanetti, Alexandre Bouchard-Côté, George Deligiannidis, and Arnaud Doucet. Scalable metropolis-hastings for exact bayesian inference with large datasets. In *International Conference on Machine Learning*, pp. 1351–1360. PMLR, 2019.
- Bo Dai, Niao He, Hanjun Dai, and Le Song. Provable bayesian inference via particle mirror descent. In *Artificial Intelligence and Statistics*, pp. 985–994. PMLR, 2016.
- Gianluca Detommaso, Tiangang Cui, Youssef Marzouk, Alessio Spantini, and Robert Scheichl. A stein variational newton method. *Advances in Neural Information Processing Systems*, 31, 2018.
- Arnaud Doucet, Will Sussman Grathwohl, Alexander G de G Matthews, and Heiko Strathmann. Annealed importance sampling meets score matching. In *ICLR Workshop on Deep Generative Models for Highly Structured Data*, 2022.
- David J Earl and Michael W Deem. Parallel tempering: Theory, applications, and new perspectives. *Physical Chemistry Chemical Physics*, 7(23):3910–3916, 2005.
- Evgenii Egorov, Ricardo Valperga, and Efstratios Gavves. Ai-sampler: Adversarial learning of markov kernels with involutive maps. In *Proceedings of the International Conference on Machine Learning (ICML)*, 2024.
- Mingzhou Fan, Ruida Zhou, Chao Tian, and Xiaoning Qian. Path-guided particle-based sampling. In *Forty-first International Conference on Machine Learning*.
- Marylou Gabrié, Grant M Rotskoff, and Eric Vanden-Eijnden. Efficient bayesian sampling using normalizing flows to assist markov chain monte carlo methods. *arXiv preprint arXiv:2107.08001*, 2021.
- Marylou Gabrié, Grant M Rotskoff, and Eric Vanden-Eijnden. Adaptive monte carlo augmented with normalizing flows. *Proceedings of the National Academy of Sciences*, 119(10):e2109420119, 2022.
- Saul Brian Gelfand, Sanjoy K Mitter, et al. On sampling methods and annealing algorithms. 1990.
- Mark Girolami and Ben Calderhead. Riemann manifold langevin and hamiltonian monte carlo methods. *Journal of the Royal Statistical Society Series B: Statistical Methodology*, 73(2):123–214, 2011.
- Jim E Griffin and Stephen G Walker. On adaptive metropolis–hastings methods. *Statistics and Computing*, 23: 123–134, 2013.
- Minghao Gu and Shiliang Sun. Neural langevin dynamical sampling. *IEEE Access*, 8:31595–31605, 2020.
- Heikki Haario, Eero Saksman, and Johanna Tamminen. An adaptive metropolis algorithm. 2001.
- Daniel C Hackett, Chung-Chun Hsieh, Michael S Albergo, Denis Boyda, Jiunn-Wei Chen, Kai-Feng Chen, Kyle Cranmer, Gurtej Kanwar, and Phiala E Shanahan. Flow-based sampling for multimodal distributions in lattice field theory. *arXiv preprint arXiv:2107.00734*, 2021.



- Paul Hagemann, Johannes Hertrich, and Gabriele Steidl. Stochastic normalizing flows for inverse problems: a markov chains viewpoint. *SIAM/ASA Journal on Uncertainty Quantification*, 10(3):1162–1190, 2022.
- Matthew Hoffman, Alexey Radul, and Pavel Sountsov. An adaptive-mcmc scheme for setting trajectory lengths in hamiltonian monte carlo. In *International Conference on Artificial Intelligence and Statistics*, pp. 3907–3915. PMLR, 2021.
- Michael F Hutchinson. A stochastic estimator of the trace of the influence matrix for laplacian smoothing splines. *Communications in Statistics-Simulation and Computation*, 18(3):1059–1076, 1989.
- Pavel Izmailov, Sharad Vikram, Matthew D Hoffman, and Andrew Gordon Gordon Wilson. What are bayesian neural network posteriors really like? In *International conference on machine learning*, pp. 4629–4640. PMLR, 2021.
- William I Jay and Ethan T Neil. Bayesian model averaging for analysis of lattice field theory results. *Physical Review D*, 103(11):114502, 2021.
- Richard Jordan, David Kinderlehrer, and Felix Otto. The variational formulation of the fokker–planck equation. *SIAM journal on mathematical analysis*, 29(1):1–17, 1998.
- Kirthevasan Kandasamy, Akshay Krishnamurthy, Jeff Schneider, and Barnabás Póczos. Parallelised bayesian optimisation via thompson sampling. In *International conference on artificial intelligence and statistics*, pp. 133–142. PMLR, 2018.
- Georgios Karagiannis and Christophe Andrieu. Annealed importance sampling reversible jump mcmc algorithms. *Journal of Computational and Graphical Statistics*, 22(3):623–648, 2013.
- Lingxiao Li, Qiang Liu, Anna Korba, Mikhail Yurochkin, and Justin Solomon. Sampling with mollified interaction energy descent. In *Proceedings of the International Conference on Learning Representations (ICLR)*, 2023.
- Tzu-Mao Li, Jaakko Lehtinen, Ravi Ramamoorthi, Wenzel Jakob, and Frédo Durand. Anisotropic gaussian mutations for metropolis light transport through hessian-hamiltonian dynamics. *ACM Transactions on Graphics (TOG)*, 34(6):1–13, 2015.
- Zengyi Li, Yubei Chen, and Friedrich T Sommer. A neural network mcmc sampler that maximizes proposal entropy. *Entropy*, 23(3):269, 2021.
- Qiang Liu. Stein variational gradient descent as gradient flow. *Advances in neural information processing systems*, 30, 2017.
- Qiang Liu and Dilin Wang. Stein variational gradient descent: A general purpose bayesian inference algorithm. *Advances in neural information processing systems*, 29, 2016.
- Bill Lozanovski, David Downing, Phuong Tran, Darpan Shidid, Ma Qian, Peter Choong, Milan Brandt, and Martin Leary. A monte carlo simulation-based approach to realistic modelling of additively manufactured lattice structures. *Additive Manufacturing*, 32:101092, 2020.
- Joel E Lynn, I Tews, Stefano Gandolfi, and A Lovato. Quantum monte carlo methods in nuclear physics: recent advances. *Annual Review of Nuclear and Particle Science*, 69(1):279–305, 2019.
- Chris J Maddison, Daniel Paulin, Yee Whye Teh, Brendan O’Donoghue, and Arnaud Doucet. Hamiltonian descent methods. *arXiv preprint arXiv:1809.05042*, 2018.
- Alex Matthews, Michael Arbel, Danilo Jimenez Rezende, and Arnaud Doucet. Continual repeated annealed flow transport monte carlo. In *International Conference on Machine Learning*, pp. 15196–15219. PMLR, 2022.
- Yinglong Miao, Victoria A Feher, and J Andrew McCammon. Gaussian accelerated molecular dynamics: unconstrained enhanced sampling and free energy calculation. *Journal of chemical theory and computation*, 11(8):3584–3595, 2015.
- Radford M Neal. Annealed importance sampling. *Statistics and computing*, 11:125–139, 2001.
- Atsushi Nitanda and Taiji Suzuki. Stochastic particle gradient descent for infinite ensembles. *arXiv preprint arXiv:1712.05438*, 2017.

- Antony M Overstall, David C Woods, and Ben M Parker. Bayesian optimal design for ordinary differential equation models with application in biological science. *Journal of the American Statistical Association*, 2020.
- Manuel Pulido and Peter Jan van Leeuwen. Sequential monte carlo with kernel embedded mappings: The mapping particle filter. *Journal of Computational Physics*, 396:400–415, 2019.
- Danilo Rezende and Shakir Mohamed. Variational inference with normalizing flows. In *International conference on machine learning*, pp. 1530–1538. PMLR, 2015.
- Benjamin Rhodes, Kai Xu, and Michael U Gutmann. Telescoping density-ratio estimation. *Advances in neural information processing systems*, 33:4905–4916, 2020.
- Enric Ribera Borrell, Jannes Quer, Lorenz Richter, and Christof Schütte. Improving control based importance sampling strategies for metastable diffusions via adapted metadynamics. *SIAM Journal on Scientific Computing*, 46(2):S298–S323, 2024.
- Lars Ruthotto, Stanley J Osher, Wuchen Li, Levon Nurbekyan, and Samy Wu Fung. A machine learning framework for solving high-dimensional mean field game and mean field control problems. *Proceedings of the National Academy of Sciences*, 117(17):9183–9193, 2020.
- Outi MH Salo-Ahen, Ida Alanko, Rajendra Bhadane, Alexandre MJJ Bonvin, Rodrigo Vargas Honorato, Shakhawath Hossain, André H Juffer, Aleksei Kabedev, Maija Lahtela-Kakkonen, Anders Støttrup Larsen, et al. Molecular dynamics simulations in drug discovery and pharmaceutical development. *Processes*, 9(1):71, 2020.
- Babak Shahbaba, Shiwei Lan, Wesley O Johnson, and Radford M Neal. Split hamiltonian monte carlo. *Statistics and Computing*, 24:339–349, 2014.
- Gregory B Sorkin. Efficient simulated annealing on fractal energy landscapes. *Algorithmica*, 6:367–418, 1991.
- Samuel Stanton, Wesley Maddox, Nate Gruver, Phillip Maffettone, Emily Delaney, Peyton Greenside, and Andrew Gordon Wilson. Accelerating bayesian optimization for biological sequence design with denoising autoencoders. In *International Conference on Machine Learning*, pp. 20459–20478. PMLR, 2022.
- Mandt Stephan, Matthew D Hoffman, David M Blei, et al. Stochastic gradient descent as approximate bayesian inference. *Journal of Machine Learning Research*, 18(134):1–35, 2017.
- Saifuddin Syed, Alexandre Bouchard-Côté, George Deligiannidis, and Arnaud Doucet. Non-reversible parallel tempering: a scalable highly parallel mcmc scheme. *Journal of the Royal Statistical Society Series B: Statistical Methodology*, 84(2):321–350, 2022.
- Yifeng Tian, Nishant Panda, and Yen Ting Lin. Liouville flow importance sampler. *arXiv preprint arXiv:2405.06672*, 2024.
- JW Van Groenigen and A Stein. Constrained optimization of spatial sampling using continuous simulated annealing. Technical report, Wiley Online Library, 1998.
- Don Van Ravenzwaaij, Pete Cassey, and Scott D Brown. A simple introduction to markov chain monte-carlo sampling. *Psychonomic bulletin & review*, 25(1):143–154, 2018.
- Linnea M Wolniewicz, Peter Sadowski, and Claudio Corti. Neural surrogate hmc: Accelerated hamiltonian monte carlo with a neural network surrogate likelihood. *arXiv preprint arXiv:2407.20432*, 2024.
- Hao Wu, Jonas Köhler, and Frank Noé. Stochastic normalizing flows. *Advances in Neural Information Processing Systems*, 33:5933–5944, 2020.
- Chen Xu, Xiuyuan Cheng, and Yao Xie. Computing high-dimensional optimal transport by flow neural networks. *arXiv preprint arXiv:2305.11857*, 2023.
- Chen Xu, Xiuyuan Cheng, and Yao Xie. Local flow matching generative models. *arXiv preprint arXiv:2410.02548*, 2024a.
- Chen Xu, Xiuyuan Cheng, and Yao Xie. Normalizing flow neural networks by jko scheme. *Advances in Neural Information Processing Systems*, 36, 2024b.

Chen Xu, Jonghyeok Lee, Xiuyuan Cheng, and Yao Xie. Flow-based distributionally robust optimization. *IEEE Journal on Selected Areas in Information Theory*, 2024c.

Guodong Zhang, Kyle Hsu, Jianing Li, Chelsea Finn, and Roger B Grosse. Differentiable annealed importance sampling and the perils of gradient noise. *Advances in Neural Information Processing Systems*, 34:19398–19410, 2021.